

# Exploring Parameter Space in Detailed Single Neuron Models: Simulations of the Mitral and Granule Cells of the Olfactory Bulb

UPINDER S. BHALLA AND JAMES M. BOWER

*Division of Biology, California Institute of Technology, Pasadena, California 91125*

## SUMMARY AND CONCLUSIONS

1. Detailed compartmental computer simulations of single mitral and granule cells of the vertebrate olfactory bulb were constructed using previously published geometric data. Electrophysiological properties were determined by comparing model output to previously published experimental data, mainly current-clamp recordings.

2. The passive electrical properties of each model were explored by comparing model output with intracellular potential data from hyperpolarizing current injection experiments. The results suggest that membrane resistivity in both cells is nonuniform, with somas having a substantially lower resistivity than the dendrites.

3. The active properties of these cells were explored by incorporating active ion channels into modeled compartments. On the basis of evidence from the literature, the mitral cell model included six channel types: fast sodium, fast delayed rectifier (K<sub>fast</sub>), slow delayed rectifier (K<sub>s</sub>), transient outward potassium current (K<sub>A</sub>), voltage- and calcium-dependent potassium current (K<sub>Ca</sub>), and L-type calcium current. The granule cell model included four channel types: rat brain sodium, K<sub>s</sub>, K<sub>A</sub>, and the non-inactivating muscarinic potassium current (K<sub>M</sub>). Modeled channels were based on the Hodgkin-Huxley formalism.

4. Representative kinetics for each of the channel classes above were obtained from the literature. The experimentally unknown spatial distributions of each included channel were obtained by systematic parameter searches. These were conducted in two ways: large-scale simulation series, in which each parameter was varied in turn, and an adaptation of a multidimensional conjugate gradient method. In each case, the simulated results were compared with experimental data using a curve-matching function evaluating mean squared differences of several aspects of the simulated and experimental voltage waveforms.

5. Systematic parameter variations revealed a single distinct region of parameter space in which the mitral cell model best fit the data. This region of parameter space was also very robust to parameter variations. Specifically, optimum performance was obtained when calcium and slow K channels were concentrated in the glomeruli, with a lower density in the soma and proximal secondary dendrites. The distribution of sodium and fast potassium channels, on the other hand, was highest at the soma and axon, with a much lighter distribution throughout the secondary dendrites. The K<sub>A</sub> and K<sub>Ca</sub> channels were also concentrated near the soma.

6. The parameter search of the granule cell model was much less restrained by experimental data. Several parameter regimes were found that gave a good match to the data. In the simplest of these, sodium and K channels were present at high density both at the soma and in the peripheral dendrites, whereas the K<sub>A</sub> and K<sub>M</sub> channels were present only in the soma.

7. Further manipulation of the mitral cell model suggests that the predicted channel distributions can be verified physiologically. If the channel distributions suggested by the model are correct, voltage clamping the soma to potentials near the spiking threshold

should result in the generation of independent local dendritic action potentials reflecting the effective decoupling of the active membranes of the different dendrites. The model predicts that the glomerular tuft, the soma, and the secondary dendrites of each mitral cell have distinct local electrical properties resulting largely from the localized distribution of ion channels. They may also be functionally distinct.

8. Our extensive search of model parameters suggests that neurons operate in regions of parameter space that are most robust to changes in parameter values. In particular, changes in channel densities by as much as an order of magnitude may have relatively little effect on the behavior of the neuronal model.

## INTRODUCTION

This paper describes an effort to model each of the two major neuronal cell classes found in the vertebrate olfactory bulb (Mori 1987). We first describe models of the mitral cell and the related tufted and displaced mitral cells. These cells provide the only bulbar output to higher centers, including piriform cortex (Haberly and Price 1977). We then present models of three classes of granule cells, which are the largest population of cells in the bulb and are involved in the centrifugal feedback from piriform cortex and other higher areas to the bulb (Mori 1987). This work extends our network modeling efforts in the olfactory cortex (Wilson and Bower 1992) to the neurons composing the brain structure that provides the primary afferent input to piriform cortex.

The pioneering modeling studies on the olfactory bulb (Rall 1970; Rall and Shepherd 1968; Rall et al. 1966) introduced multicompartmental models of the mitral and granule cells. These consisted of 5–10 compartments and involved reduced (FitzHugh 1961) active properties. These single-cell and network models were consistent with many of the experimental details available at the time, and demonstrated the power of simulation techniques as a means for understanding physiological observations. The accumulation of much more detailed experimental data on these cell types and the availability of vastly greater computational resources makes it possible to now model the cells in considerably more detail. As with the original modeling studies, the development of single cell models is a necessary prelude to a detailed model of the bulb as a whole.

As is the case with most modern efforts to model single neurons (De Schutter and Bower 1991; Segev et al. 1990; Woolf et al. 1991a), the approach taken here involved first constructing an anatomically correct compartmental representation of each neuron of interest and then studying the passive properties of the model. Active channels were sub-

sequently incorporated into the passive model on the basis of evidence from the literature for the presence of particular channel types. Parameters such as channel densities and kinetics were then varied to replicate previously published physiological response properties.

As is also the case for most detailed single-cell models, values for many of the parameters of interest, especially ion channel densities and channel kinetics, are not available directly from conventional experimental data such as intracellular somatic recordings (Koch and Bower 1992). Traditionally, models have either relied on additional data (calcium imaging, dendritic recordings) or have involved estimates of channel properties that lack quantitative precision. It has usually been an open question as to whether the particular parameter values selected are the only viable parameters or just one of several possible solutions. This issue becomes more serious as models become more realistically detailed and the number of parameters increases.

In this paper, we have employed a systematic and semiautomated method to explore possible parameters for models of the two major types of olfactory bulb neurons and their subclasses. These extensive searches of parameter space were performed on a parallel supercomputer, the Touchstone Delta at Caltech. In the case of the experimentally well-studied mitral cell, we have discovered a single region of parameter space in which the similarity of model output and experimental data is preserved for a fairly large range of most parameter values. In fact, some parameters allow up to an order of magnitude of leeway around the optimal value. The robust behavior of this cell model suggests that real neurons may seek to operate in regions of parameter space that are tolerant of small or even sizable changes in their physical characteristics (e.g., channel densities). This may have important implications for the robustness of the nervous system to small differences during development, to damage, and to the many environmental changes that are known to affect the detailed properties of ion channels.

In the case of the less well-studied granule cell, several equivalent regions of parameter space have been found. These results demonstrate the importance of experimental data as constraints on model parameters, as well as the utility of careful studies of parameter space as a guide to future experimental work.

## METHODS

### *General simulation procedures*

The models described here are all in the class of single neuron models in which neuronal structure is represented as a series of electrically linked compartments (Cooley and Dodge 1966; Rall 1964).

In general, the same modeling approach was taken to construct and parameterize each of the models discussed in this paper. In each case, the first step was to establish the overall compartmental structure of the model on the basis of previously published quantitative descriptions of cellular anatomy. Once an anatomically accurate model was constructed, the passive electrical properties of the cells were established. Finally, active properties were explored by adding ionic conductances to the different compartments.

As described in the introduction, the principal effort in model-

ing these cells involved finding parameter values that produce model behavior consistent with experimental results. In some cases, good estimates of parameters can be obtained from the literature, e.g., cellular anatomy or the presence of certain channel types. In other cases (channel distributions or kinetics), information is either difficult to obtain or not available. For channel kinetics, we used parameters determined for other neuronal types, as described below. Values for channel densities were estimated on the basis of parameter searches that compared model output to physiological records, which are relatively easy to obtain experimentally.

Our models utilize parameters from many different sources and species. This is necessitated by the lack of complete data from any one species. In particular, the cell geometry is based largely on mammalian data and is scaled to correspond to the size of nominal rabbit neurons. The electrophysiological data are largely (but not exclusively) from turtle, because that preparation has proven most amenable to detailed single-cell analysis of the sort required. As we shall discuss for specific instances, in most cases we do have comparable data from turtle, rabbit, and other species. This provides bounds on the expected variability in properties, and in most cases demonstrates a high level of consistency between species. The judicious use of data from several sources is common in modeling studies where experimental data on the system under study are inadequate (e.g., combining channel density information: Beluzi and Sacchi 1991; channel kinetics: Yamada et al. 1989). For many well-defined neuronal classes, a single canonical model is expected to provide a good representation for a particular neuron type over a fairly wide range of species and brain regions (Shepherd 1992).

### *Source of known parameters*

**ANATOMIC ORGANIZATION.** The morphological data used to obtain the basic structure of each cell type was taken primarily from rabbit (Mori et al. 1983), but also from mouse (Greer 1987) and rat (Price and Powell 1970a,b). These studies reveal that the morphology of the cells in the olfactory bulb is remarkably consistent among vertebrates (Mori 1987), the main difference being one of scale. The specific model for each cell type was constructed by averaging published values for soma size, length of interbranch segments, diameter of branches, branching probabilities, and density and size of any spines.

**PASSIVE PROPERTIES.** Once the anatomic organization of a particular model was established, basic parameters governing the passive electrical properties of each cell type were added to the model. Membrane capacitance ( $C_m$ ) and axoplasmic resistivity ( $R_a$ ) have fairly consistent values in the literature (Jack et al. 1983). For the models described here, the  $R_a$  was set at 50  $\Omega\text{cm}$  (granule cell) and 200  $\Omega\text{cm}$  (mitral cell).  $C_m$  was taken to be 1.0  $\mu\text{F}/\text{cm}^2$ . Membrane resistivity ( $R_m$ ) is more difficult to measure experimentally (Jack et al. 1983; Rall 1959), and therefore was determined in the current models by matching intracellular current-clamp data using hyperpolarizing pulses (Jahr and Nicoll 1982; Mori et al. 1981a). Values used for  $R_m$  were made uniform throughout the dendritic structure but lower at the soma. This modification was intended to take into account the leak due to damage caused by the somatic recording electrode (Pongracz et al. 1991; Segev et al. 1990). When comparing published time courses and input resistances to simulated data, charging curves were fitted with a two-exponential curve using the Levenberg-Marquardt (nonlinear least-squares) method (Press et al. 1988).

**ACTIVE CHANNEL PROPERTIES.** The identities of the channels included in each model were inferred from the published effects of specific channel blockers on the electrical properties of each cell.

Good data on this subject exists for the mitral cell, but less data is available for the granule cell. Accordingly, fewer channel types were assumed to exist for the latter case (see below).

Determining appropriate channel kinetics is a somewhat more complex process in that detailed descriptions of channel kinetics are not available for these specific cell types. The starting points for channel kinetic parameters were therefore derived from the values for similar channels in other cell types. In this study, initial channel kinetics were obtained from a wide variety of sources and then implemented in Hodgkin-Huxley (Hodgkin and Huxley 1952) form as discussed below in detail for each cell type.

In principle, the parameter search approach could also be applied to the channel kinetics. This was not done in this study for the following reasons. First, each channel requires the specification of as many as 18 kinetic parameters: 4 for each of the forward and backward rate functions in each of the two gates, plus a power term for each gate. (see APPENDIX C: CHANNEL PARAMETERS). This would be difficult to handle with the present parameter search methods (APPENDIX B). Second, neuronal properties tend to be very sensitive to variations in channel kinetics, unlike their more robust behavior with channel densities. Finally, an unconstrained automatic search could potentially distort channel properties beyond the range normally expected for their channel class. Given the availability of well-described channels of the desired classes from other systems, we chose to base our channel kinetics more directly on data from the literature.

### *Unknown parameter estimation*

In general, the properties of each cell depend, in varying degrees, on a vast number of parameters, many of which are not known in detail or at all for the cells modeled here. In active cell models, the number of such free parameters is enormous. For example, information on channel distributions and densities is not yet readily available for each channel type, but is critical to model behavior. Accordingly, possible values for the spatial distribution of channels must be explored by matching model output to existing physiological data. Simplifying assumptions must be made to reduce the number of degrees of freedom in a complex neuronal model (Rall 1990) to a tractable range in a systematic manner.

We have adopted the following basic approach to defining the parameter space of our models: first, we establish as many model parameters as we can in an unambiguous manner. This includes the morphology, passive properties, and a minimal set of  $X$  channel types that would be consistent with the data. These parameters are then held fixed. Second, we subdivide the model into  $Y$  distinct regions within which the channel distributions are assumed to be uniform. For each of these regions, we assign the entire set of channel types. This establishes our basic parameter space of  $X \times Y$  dimensions. Finally, when the parameter search indicates that certain channel classes may not play a significant role in a given region, those channels are eliminated from that region of the model.

We have found that the process just described can readily be automated if two conditions can be met. First, there must be a means of evaluating the "goodness" of a particular set of parameters. Second, there must be a mechanism for systematically sampling parameter space. The approach used here to accomplish these two objectives is described in more detail in APPENDIX A and APPENDIX B.

### *Mitral cell parameters and variations*

**ANATOMIC ORGANIZATION.** Three classes of mitral cell models were constructed: mitral, displaced mitral, and tufted cells. Very

good statistical information is available on the morphology of these cells (Mori et al. 1983; Price and Powell 1970a,b).

**MATCHED PHYSIOLOGICAL DATA.** Electrophysiological data from current-clamp experiments in the turtle mitral cell (Mori et al. 1981a, 1982) were the main source of physiological data used in this study. Turtle mitral cells frequently have more than one primary dendrite (Mori 1987), but are otherwise similar in geometry to their mammalian counterparts. Whole-cell current-clamp recordings from mammalian mitral cells have been made (Bufler et al. 1992, Nickell et al. 1992) in the slice, and have qualitatively similar appearance to the turtle recordings. However, the very large mitral cell dendritic arborization is invariably damaged in slice preparations, which makes the data hard to interpret. Spike thresholds appear to be in the same range as for the turtle data, but the resting potential for the whole-cell recordings is approximately  $-80$  mV (Bufler et al. 1992), which is 15 mV lower. Whole-cell current-clamp recordings from mitral cells in primary cultures of mammalian olfactory bulb (Trombley and Shepherd 1992) also show very similar voltage waveforms to the turtle recordings.

Further evidence for the similarity in electrophysiological properties of mitral cells in turtle and mammals is available from intracellular recordings under a variety of stimulus conditions. Fast prepotentials that can be isolated by hyperpolarization are evident in responses to olfactory nerve stimulation in rabbit (Mori and Takagi 1975) and turtle (Jahr and Nicoll 1982; Mori et al. 1982). Similar fast prepotentials have been reported in rats (Wellis et al. 1989) in the absence of hyperpolarization. In all cases, these prepotentials are interpreted as originating from apical dendritic spikes. Close correspondence between turtle (Jahr and Nicoll 1982; Mori et al. 1981a) and rabbit (Mori and Takagi 1975, 1978) is also seen in experiments where the lateral olfactory tract is stimulated and intracellular recordings made from the mitral cell soma. In each case, a distinctive sequence of M, A, and B spikes is observed, which is interpreted as the successive activation of the myelinated axon (M), the axon hillock (A), and the somadendritic membrane (B). On the basis of these observations, a strong case can be made for similarity in mitral cell active properties across vertebrates, and specifically between rabbits and turtles, which provide much of our morphological and electrophysiological data, respectively.

**CHANNEL TYPES.** A large amount of data is available on the types of channels found in mitral cells. Blockage of fast spikes by tetrodotoxin (TTX) (Jahr and Nicoll 1982; Mori et al. 1981a, reproduced in Fig. 4A below) shows the presence of sodium channels (Na). Blockage of the remaining spikes using cobalt ions (Jahr and Nicoll 1982; Mori et al. 1981a) reveals a calcium current [modeled as an L-type calcium current (LCa)]. The situation with potassium currents is, as is frequently the case, less distinct. The rapid repolarization after the action potential (Fig. 4A) makes it clear that a fast delayed rectifier (Kfast) is present. In addition, the somewhat less rapid hyperpolarization (Fig. 4A) after the calcium spike in the presence of TTX and tetraethylammonium (TEA) suggests a remaining slower, delayed rectifier current (K). The slow rate of charging of the membrane (Fig. 4A) when current is being injected suggests that an anomalous rectifier current (KA) is active. Both calcium- and sodium-dependent K channels have been shown to exist in the mitral cell (Egan et al. 1992; Jahr and Nicoll 1982). The presence of cation-dependent K currents can also be deduced from the increase in interspike interval after the first spike induced with current injection (Mori et al. 1981a, Fig. 4, A and D). We have chosen to model the calcium-dependent K channel (KCa) because the whole-cell experiments do not reveal sodium-dependent currents except at very high concentrations of sodium (Egan et al. 1992). Accordingly, four classes of K channels were modeled: Kfast, slow K, KA, and KCa. Under

the experimental conditions of channel block (10 mM TTX, 5 mM TEA, see Mori et al. 1981a), Kfast channels are likely to be completely blocked, slow K channels partially blocked, and the KA and KCa channels not much affected (Connor and Stevens 1971).

**CHANNEL KINETICS.** The following final set of channels were used in the mitral cell model: 1) fast Na (slightly modified from Traub 1982); 2) Kfast, 3) K (both modified from Adams et al. 1980 and Aldrich et al. 1979); 4) KA (Yamada et al. 1989); 5) LCa (modified from De Schutter 1991 and Hirano and Hagiwara 1989); and 6) KCa (modified from Traub 1982). The calcium dependence of this last channel was modeled by establishing a single pool of intracellular calcium, which decays after calcium channel activation to a baseline of 10 nM with a single time constant of 10 ms. Accordingly, calcium influx is assumed to be due only to the action of the LCa current, and lateral diffusion of calcium is not modeled.

Most of the selection of appropriate channels and kinetics was done on a single-compartment model by varying the channel parameters under conditions of current clamp using the "Neurokit" tool in the GENESIS script libraries (Wilson et al. 1989). This more readily allowed the comparison of modeled voltage traces with experimental data. Channels tuned in this manner were then incorporated into the full mitral cell model for further evaluation.

**SPATIAL DISTRIBUTION OF CHANNELS.** Channel density distributions have not been directly measured in mitral cells, but numerous experiments (e.g., Jahr and Nicoll 1982; Mori and Takagi 1975; Mori et al. 1982) suggest the presence of active channels distributed over various parts of the mitral cell dendritic arbor. In the absence of direct data on channel densities, a very conservative approach was taken to estimating these parameters. Six regions of the cell were considered as having distinct channel densities: the soma, primary dendrite, glomerular tuft, proximal secondary dendrites, distal secondary dendrites, and axon (see Fig. 3 below). Within each region, a uniform distribution was assumed.

The availability of current-clamp records in the presence of applied blockers (Jahr and Nicoll 1982; Mori et al. 1981a) is very valuable for constraining the parameter search process. Under blockage of Na channels by TTX and Kfast by TEA, we can conduct a parameter search with these channels missing from each of the six regions of the mitral cell, resulting in a far more tractable 24 parameters. Having fixed more than half of the model parameters using this initial parameter search, finding channel densities for the unblocked model involved a much smaller parameter space. Further refinement was possible for special cases where additional information was available. For example, the experimentally demonstrated propagation of antidromic spikes into the mitral cell soma (Mori et al. 1981a, 1982) requires a higher channel density in the axon initial segments than in the rest of the axon.

**OTHER CLASSES OF MITRAL CELLS.** In general, displaced mitral and tufted cells are believed to have similar properties and functions to the more extensively studied mitral cells (Mori 1987). It has therefore been assumed that the channel kinetics and density parameters obtained for the mitral cells apply directly to the different geometries (Mori et al. 1983) of these other cell types. It has also been reported that a small percentage of mitral cells in mammalian olfactory bulb have two primary dendrites (Mori et al. 1983). As mentioned previously, multiple primary dendrites are quite common in turtle and amphibian mitral cells (Mori et al. 1981a), which are the source of much of the physiological data used in these simulations. Accordingly, channel properties and distributions from the basic mitral cell model were also tested in additional models with the geometries appropriate to the tufted, displaced mitral, and turtle mitral cells.

### *Granule cell parameters and variations*

**ANATOMIC STRUCTURE.** Three types of previously described granule cells were also modeled: type I, type II, and type III. Morphological data is available from several species: rabbit (Mori and Kishi 1982; Mori et al. 1983), rat (Price and Powell 1970a), and mouse (Greer 1987, Woolf et al. 1991a,b). The convoluted morphology that the above studies reveal in granule cell dendrites was taken into account by increasing the equivalent membrane area by a factor of 2.0. Granule cell spines were simulated by assigning each model the same number and spatial distribution of spines as reported in the literature (Mori et al. 1983). All spines consisted of identical neck and head compartments (Shepherd and Brayton 1987), with no attempt being made to include the considerable anatomic variability in spine morphology that has previously been reported (Woolf et al. 1991a,b).

**MATCHED PHYSIOLOGICAL DATA.** The difficulty of obtaining stable intracellular recordings in the granule cell has limited the amount of data available for assessing the detailed electrical properties of the granule cell (Jahr and Nicoll 1982; Mori and Kishi 1982; Wellis and Scott 1990). For the same reason, there is also a lack of information on the effects of channel blockers during current injection. Accordingly, a limited set of channels was used for simulating granule cell spikes (see below). An additional complication in the data for hyperpolarizing current injections used in the "passive" granule cell model was a large (2-fold) discrepancy in the time courses for charging and repolarization of the cell. This issue is dealt with in the DISCUSSION. Recordings from current injection experiments in rat (Wellis and Scott 1990) and turtle (Jahr and Nicoll 1982) show substantial similarity in spike waveforms, suggesting that it is reasonable to combine morphological and electrophysiological data from these different sources.

**CHANNEL TYPES.** Granule cell spikes were assumed to be due to Na and potassium channels on the basis of the Hodgkin-Huxley formalism. On the basis of the previously reported increasing interval between spikes during the depolarizing current pulse (Jahr and Nicoll 1982), an additional noninactivating muscarinic K channel (KM) was incorporated into the model. The kinetics and spatial distributions of these channels were varied to obtain matches to the experimental data that do exist for depolarizing current clamp (Jahr and Nicoll 1982).

**CHANNEL KINETICS.** The library of channels assembled in GENESIS was used to select channels that satisfied the slower kinetics seen in the granule cell data. The following final set of channels was used in the granule cell models: rat brain Na ( $Na_{gran}$ ) (Stuhmer et al. 1987), modified K (Adams et al. 1980; Aldrich et al. 1979), and the bullfrog sympathetic ganglion neuron KM and KA channels (Yamada et al. 1989).

**SPATIAL DISTRIBUTION OF CHANNELS.** A similar analysis was applied to the granule cell channel distribution as with mitral cells. In this case, only four channels were considered. The regions of the granule cell considered as electrically distinct were: soma, trunk, peripheral processes, and the descending (deep) dendrites (see Fig. 6 below). Additional simulations also considered the possibility of ion channels in the spines. Simulations were performed while varying channel densities over each of these regions. The parameter searches revealed several distinct channel distributions that adequately matched experimental data.

**OTHER CLASSES OF GRANULE CELLS.** Three types of previously described granule cells were modeled: type I, type II, and type III (Greer 1987; Mori et al. 1983). As with the mitral cell types, it was assumed for simplicity that the basic channel properties and distributions in each granule cell type are the same and that the only variation in classes was morphological. The channel distribution



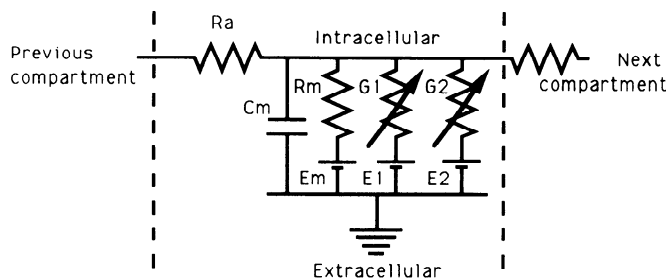


FIG. 1. Circuit diagram for compartmental model. Following the classical description of an active compartment (Rall 1959), it is represented as a membrane resistance ( $R_m$ ) in parallel with a membrane capacitance ( $C_m$ ), and an axial resistance ( $R_a$ ) that combines the cytoplasmic and extracellular axial resistance. The channel conductances are represented as variable conductances ( $G_1$ ,  $G_2$  and so on) in parallel with the  $R_m$ . Each of the transmembrane conductances ( $R_m$ ,  $G_1$ ,  $G_2$ , etc.), is in series with the appropriate potential. These potentials are derived from the reversal potentials for the ions passing through the conductance, and are kept fixed in these models.

from the simplest (least number of channels/compartments) type I model was applied to the type II and type III cells.

### Computational issues

**SIMULATION ENVIRONMENT.** All simulations were performed on the GENESIS simulator developed at Caltech (Wilson et al. 1989). Interactive simulations and parameter variations were performed using a special single-cell simulation tool within GENESIS called Neurokit. As described in APPENDIX B, exhaustive parameter searches were performed in batch mode under the control of GENESIS script language programs. The library of ion channels that has been constructed within GENESIS on the basis of data in the literature was used extensively during these simulations. Initial simulations were performed on a variety of UNIX workstations, whereas extensive parameter variations have employed the Intel Touchstone Delta parallel supercomputer at Caltech.

**NUMERICAL TECHNIQUES.** Implicit (Backward Euler, Crank Nicolson) as well as explicit (forward exponential Euler) integration methods were used to evaluate the systems of coupled differential equations that arise from the compartmental modeling scheme (Fig. 1). In both cases, the time step was empirically chosen so that the change in interspike interval with a halved time step was  $<0.5\%$ . Typical time steps used were  $50 \mu s$  using the implicit method and  $5 \mu s$  for the explicit method. In the case of granule cells, however, the presence of numerous spines renders the system of equations numerically very stiff, and time steps of  $20 ns$  were required for accuracy when using the explicit method.

The Hines numbering scheme (Hines 1984) was used to reduce the number of operations for solution using the implicit method and Gaussian elimination, to the order of the number of compartments; Hodgkin-Huxley equations were evaluated in the implicit method on a staggered time grid (Hines 1984; Mascagni 1989) to obtain second-order accuracy, except for the calcium-dependent potassium channels. The more complex form of these channels (Traub 1982; see APPENDIX C) necessitated the use of the explicit method in their evaluation. This combination of integration methods did not lead to serious difficulties, because the relevant time constants were an order of magnitude slower than the time step.

Simulations performed using the implicit and explicit methods were checked against each other to verify consistency. The accuracy of these solutions was further confirmed by simulation of a constant-current injection to obtain the input resistance of the cell from the asymptotic potential. The input resistance was then di-

rectly calculated using Ohm's Law and the circuit equivalent of the cell and found to be identical with the previous estimate. Additional comparisons were made with values for input resistance calculated using full cable theory (Jack et al. 1983; Rall 1959; Rall and Rinzel 1973). These differ slightly because of the compartmental approximations, with the difference depending on the size of the compartments. In a 286-compartmental model of the mitral cell, where all compartments are smaller than  $0.02$  length constants, the difference is  $<1\%$ .

The Hodgkin-Huxley equations were implemented using a tabulated lookup scheme, with a large number of sample points (every  $50 \mu V$ ) to retain numerical accuracy (Hines 1984; Mascagni 1989). The use of tables permits one to directly utilize experimental curves for voltage dependencies without resorting to curve-fitting. Additionally, it is computationally much more efficient than calculating exponentials. In cases where the curves were directly taken from published data, the limited number of experimental data points were interpolated using Bezier splines (Enns 1986) to obtain sufficient sample points for the table.

The correctness and accuracy of the GENESIS simulator as a whole has been evaluated using the Rallpack set of benchmarks (Bhalla et al. 1992). Briefly, the accuracy benchmarks calculate the normalized root-mean-squared difference between the simulated and the correct voltage waveform for a particular model. The Rallpack axon model incorporates Hodgkin-Huxley-type channels in a 1,000-compartment cylindrical membrane and is appropriate for testing simulator performance for active models of the kind discussed in this study. At the time steps used in these simulations, the error for the axon model in the Rallpacks is  $1.3\%$ .

### Parameter availability

All model parameters are available from the authors or by ftp from Babel, the GENESIS users' group. Scripts for running these simulations within the GENESIS environment are also available from the same source. Inquiries should be addressed to [babel.cns.caltech.edu](mailto:babel.cns.caltech.edu).

## RESULTS

In the course of this study, a great number of parameter variations were explored while comparing model output to physiological data. In the following sections, the resulting final state of each neuronal model will be presented. In each case, the final parameters were determined on the basis of two criteria: first, the ability of the resulting model to replicate physiological data as evaluated by the curve-matching function. Second, the robustness of the model as determined by varying parameters in the vicinity of the final solution and observing how well the simulations continued to match experiment. In terms of the curve-matching function, this translates to smoothness of the function in the region of the best match (Fig. 2).

Although it is very likely the case that some other more complicated combination of channels, channel kinetics, and/or channel distributions could meet the same criteria, we will describe the simplest combination of parameters that our models suggest satisfy the data. After the description of the final models, we then describe a number of manipulations performed on them to explore their behavior in various physiological and experimental contexts.

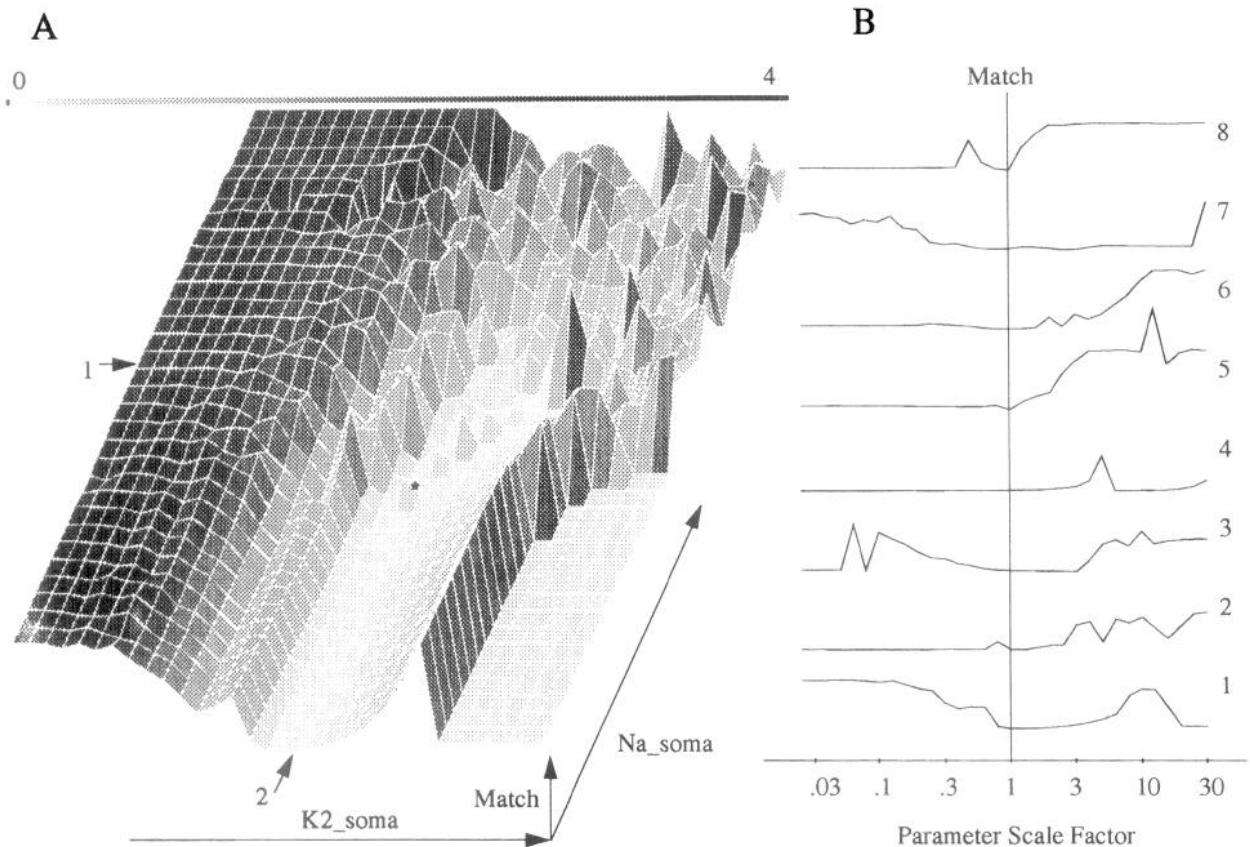


FIG. 2. Parameter space for selected parameters of the mitral cell model. *A*: 2-dimensional plot of a plane section through parameter space. Shading and vertical axis; match value, which is 0 for a perfect match. *X* and *Y* axes (labeled K2\_soma and Na\_soma): scale factors for the densities of the fast potassium (Kfast) current in the soma, and the sodium (Na) current in the soma, respectively. Each grid division is a factor of  $2^{1/3}$  ( $\sim 1.26$ ) larger than the previous one. The range of the axes is from  $2^{-19/3}$  to  $2^{19/3}$ . Asterisk: location of the final model in parameter space (corresponding to a scale factor of 1 for all parameters). The indicated lines 1 and 2 correspond to traces 1 and 2 in *B*. *B*: variation of the match value when the density of a single channel is varied away from that of the final model. 1 to 6 are channels in the soma: Kfast, Na, Ca, slower delayed rectifier current (K), anomalous rectifier current (KA), and calcium-dependent K current (KCa). 7: sodium in proximal secondary dendrites. 8: calcium in the glomerular tuft. All match values in *A* and *B* were calculated using the same set of weighting factors for the waveform-matching function (APPENDIX A). Different weighting factors produce qualitatively very similar curves. Complete sets of parameter match values can be obtained from the authors.

### Mitral cells

**PASSIVE PROPERTIES.** Hyperpolarizing current injections into the mitral cell produce charging curves with two time constants (Mori et al. 1981a; Rall 1969) and provide an estimate for the cell's input resistance and electrotonic length. The model replicates these results when somatic  $R_m$  is lower than for the rest of the cell. As has been previously reported, (e.g., motoneurons: Segev et al. 1990; hippocampal granule cells: Yuen and Durand 1991), such a "step model" for  $R_m$  is consistent with the existing experimental data. The model is tuned to replicate the 60-M $\Omega$  input resistance reported for turtle mitral cells (Mori et al. 1981a) impaled by an intracellular electrode. This input resistance is higher than that obtained in intracellular recordings from other systems (e.g., cat spinal motoneurons: Rall 1977; hippocampal pyramidal cells: Schwartzkroin 1978). However, this upward revision is consistent with a trend toward higher estimates of  $R_m$  based on patch-electrode recordings (Staley et al. 1992). When one removes this "leak conductance" from the model and sets the somatic resistivity equal

to that for the rest of the cell, the model predicts an input resistance of 120 M $\Omega$ . This figure is comparable to those obtained using whole-cell patch-electrode recordings in salamander mitral cells (D. P. Wellis, personal communication) and in the rat olfactory bulb slice preparation (Nickell et al. 1992). The passive parameters for the final models for the mitral cell and its subclasses were: axial resistivity = 2.0  $\Omega\text{m}$  = 200  $\Omega\text{cm}$ ; membrane resistivity = 10.0  $\Omega\text{m}^2$  = 100,000  $\Omega\text{cm}^2$ ;  $C_m$  = 0.01 F/ $\text{m}^2$  = 1.0  $\mu\text{F}/\text{cm}^2$ . Electrode damage was modeled as a leak conductance of 120 M $\Omega$ .

**CHANNEL DISTRIBUTIONS.** The final mitral cell model has 718 channels; on average, 2.5 channels per compartment (Fig. 3).

*Fast Na and K.* These two channels are differentially distributed, with the highest density occurring in the soma and axon initial segments (see Table 1). Previous modeling studies involving mitral cells (Rall 1970; Rall and Shepherd 1968) have incorporated corresponding spiking mechanisms in the axon and soma. High channel densities in these regions are in agreement with the classical description of a neuron and are required to replicate the sequence of M,

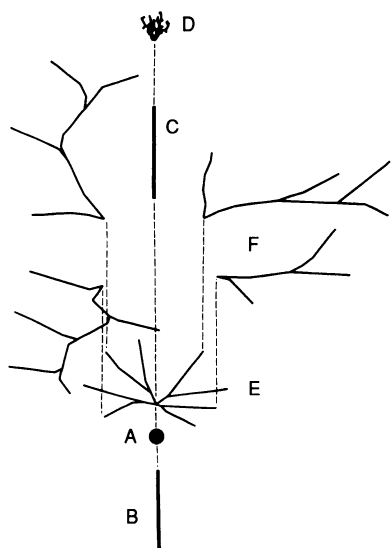


FIG. 3. Regions for mitral cell parameter variations. The cell was subdivided into 6 regions, A–F. A, soma; B, axon; C, primary dendrite; D, glomerular tuft; E, proximal secondary dendrites; F, distal secondary dendrites. As described in the text, these regions were the basis for parameter variations. Within each region all channel densities are uniform, except for the axon. In the axon, the channel densities near the soma were greater, but the densities were always varied by a uniform scaling factor when doing parameter variations. The final values for channel densities are given in Table 1.

A, and B spikes during antidromic activation of the mitral cell. This spike sequence is interpreted as the successive activation of the myelinated axon, the axon initial segment, and the somadendritic membrane (Jahr and Nicoll 1982; Mori and Takagi 1975, 1978; Mori et al. 1981a). As discussed in previous studies on olfactory bulb models (Rall 1970; Rall and Shepherd 1968), there is an impedance mismatch between the thin axon and the much larger soma that may lead to failure of antidromic spike propagation. Our study explicitly models the axon initial segment as a succession of short compartments with diameter increasing to match that of the soma, and with large Na- and K-channel densities. This leads to a satisfactory replication of experimental data relating to various phases of antidromic spikes. With respect to the dendrites, neither of these channels were included in the primary dendrites and glomerular

TABLE 1. Mitral cell channel distributions

Region	Na	Kfast	LCa	K	KA	KCa
Soma	1,532	1,956	40	28	58.7	142
Axon*	4,681	1,541	20	15.5	51.5	88.7
Primary dendrite	13.4	12.3	22	17.4	0	0
Glomerular tuft	0	0	95	28	0	0
Proximal secondary dendrite	330	226	4	8.5	0	0
Distal secondary dendrite	122	128	0	0	0	0

Channel densities are expressed as Siemens per square meter for the maximum conductance value  $\bar{g}$  in the rate equation for the channel. Na, sodium channels; Kfast, fast delayed rectifier current; LCa, L-type calcium current; K, slower delayed rectifier current; KA, anomalous rectifier current; KCa, calcium-dependent K channel. \*Channel densities on the axon varied between compartments; the values for the most proximal are given.

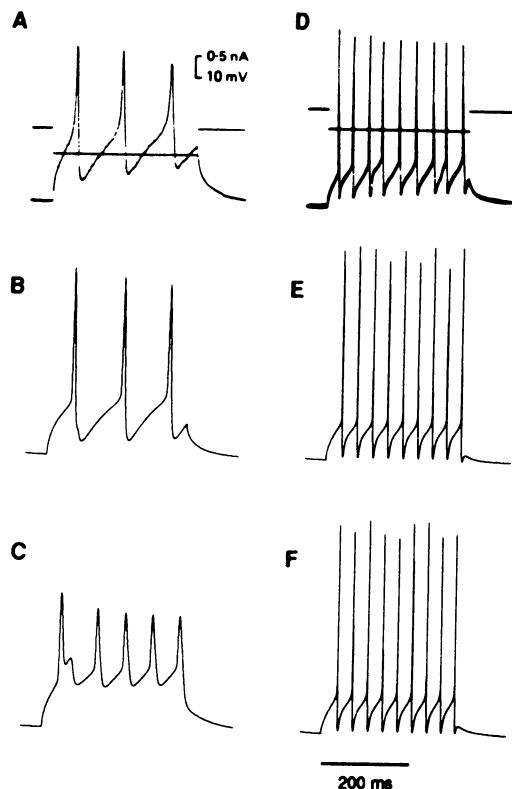


FIG. 4. Experimental and simulated data for mitral cell. A: current-clamp recordings from mitral cell in the presence of  $10^{-5}$  M tetrodotoxin (TTX) and  $5 \times 10^{-3}$  M tetraethylammonium (TEA), injection current = 0.62 nA (reproduced with permission from Mori et al. 1981a). B: simulated results under same conditions as A. The larger amplitude of the simulated spikes may be due to high-frequency cutoff in the recording apparatus. The model also uses a fixed calcium reversal potential of +70 mV that fails to take into account the lowered Nernst potential during the spike. C: simulated results when model is without calcium in soma and vicinity. D: current-clamp recordings from mitral cell with injection current of 0.5 nA. (Reproduced with permission from Mori et al. 1981a.) E: simulated results under same conditions as D. The same factors as in B may affect spike height and width. F: simulated results without modeled electrode damage. Current injection = 0.4 nA to compensate for increased input resistance of cell as compared with E.

tufts, but the best match to the observed spike waveforms required the inclusion of both at a lower but significant density in the secondary dendrites. Again, this is consistent with the earlier studies (Rall 1970; Rall and Shepherd 1968) where it was found that active dendritic compartments supported the rapid depolarization of the dendrites following antidromic spike invasion.

**KA and KCa.** The KA and KCa channels are present only in the soma and axon initial segments in our model. The simulations accurately reproduced experimental data for current injection in the presence of TEA and TTX with this simple arrangement (Fig. 4A).

**Ca and slow K.** The Ca and slow K channels are present everywhere except in the distal secondary dendrites. They are most concentrated in the glomerular tuft, at a lower density in the primary dendrite and soma, and still lower in the proximal secondary dendrites. This broad distribution gives a good approximation to experimental data (Fig. 4A) and also emerges from two additional considerations. First, it is known from experimental studies (Jahr and Nicoll

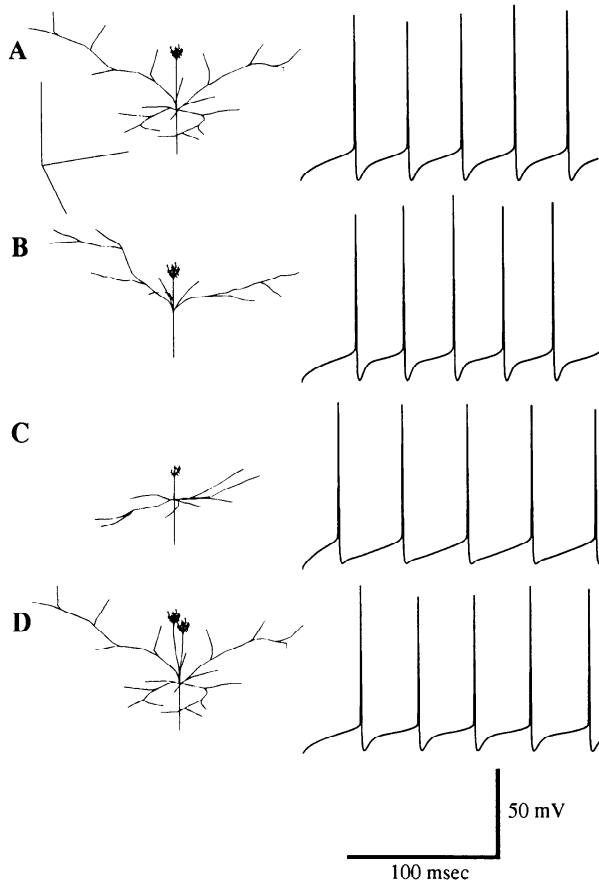


FIG. 5. Different classes of modeled mitral cell. All models have assumed electrode leak at soma of 120 M $\Omega$ . *Left* column: cell geometries. Scale bars are 1 mm on each axis. *Right* column: somatic recordings in response to current injection. *A*: mitral cell, 0.5-nA current injection. *B*: displaced mitral cell, 0.4-nA current injection. *C*: tufted cell, 0.35-nA current injection. *D*: turtle mitral cell with 2 primary dendrites, 0.75-nA current injection.

1982; Mori and Takagi 1975; Mori et al. 1982; Wellis et al. 1989) that fast prepotentials occur when the olfactory nerve is stimulated. This pathway synapses onto the glomerular region, which would therefore be a good candidate for the site of the prepotentials. Second, concentrating calcium channels in the glomerular tuft alone is inconsistent with the large, sharp calcium spikes seen under current clamp in the presence of TEA and TTX (Fig. 4, *A* and *C*).

Figure 4 compares experimental and simulated voltage traces obtained with this channel distribution. It can be seen that there is a good overall match between simulated and experimental results.

**APPLYING CELL PARAMETERS TO OTHER CLASSES OF MITRAL CELLS.** The passive properties and channel distributions obtained for the mitral cell model above were adapted to the other types of mitral/tufted cells studied. This process involves subdividing the cell into compartments according to their geometry, as was done for the mitral cell, and then placing similar channel densities in regions of the cells corresponding to the already calculated mitral cell model.

All four mitral cells produce similar sharp spikes with afterhyperpolarizations (Fig. 5) and show similar patterns of propagation of spikes into the secondary dendrites (see

Fig. 11 below). This result, however, is highly dependent on the assumption of similar distributions of ion channels. One apparent difference between the cells is the latency to the first spike after current injection. This is due to the differences in passive properties of the cells (particularly input resistance and equalizing time courses), which is strongly dependent on cell geometry. The modeled data generally match the experimental data in this regard.

There is notable similarity in spike waveform (Fig. 5), passive properties (Table 2), and the details of spike propagation into dendrites (Fig. 11, turtle data is very similar) between the mitral cell and the "turtle" mitral cell. Overall, the simulations reflect experimental findings, suggesting a close correspondence between rabbit and turtle mitral cell properties.

### Granule cells

**PASSIVE PROPERTIES.** There is very limited information available for direct estimation of granule cell passive properties (Jahr and Nicoll 1982). Previously published data do, however, indicate a two-fold difference in time course between hyperpolarizing and repolarizing phases of a current pulse (Fig. 8*A*).

In the passive granule cell model, we have chosen to replicate the voltage trace of only the repolarizing phase because this is less likely to be contaminated by ion currents. Only one distinct time constant could be extracted from the available data. We have fitted this data using a similar assumption, as for the mitral cell, that there is a constant  $R_m$  and an additional leak conductance in the soma due to the electrode. The values obtained for these parameters were 12  $\Omega m^2 = 120,000 \Omega cm^2$  and 200 M $\Omega$ , respectively. The other passive properties were axial resistivity = 0.5  $\Omega m = 50 \Omega cm$  and  $C_m = 0.01 F/m^2 = 1.0 \mu F/cm^2$ .

**CHANNEL DISTRIBUTIONS.** The parameter searches for the granule cells came up with three distinct sets of parameters (Figs. 7 and 8) that provide a good match to experiment. It seems likely that there are many possible channel distributions that may fit the limited amount of available data. We describe the simplest set of parameters we found, in which the model has the smallest number of channels per compartment (Table 3).

The number of Hodgkin-Huxley type channels in the final model of the type I granule cell is 162. These are distributed among 944 compartments. None of the channels are

TABLE 2. *Mitral cell model properties*

Cell	<i>n</i>	<i>nC</i>	$\tau_0$ , ms	$\tau_1$ , ms	<i>L</i>	$R_{input}$ , M $\Omega$
Mitral	286	718	59	6.2	1.1	60.9
Displaced mitral	220	520	51	5.4	1.1	73.0
Tufted	133	331	36	3.6	1.0	84.6
Turtle	386	930	70	7.0	1.0	53.7

*n*, number of compartments; *nC*, number of channels;  $\tau_0$ , first (charging) time constant of cell;  $\tau_1$ , second (equalizing) time constant of cell; *L*, length of cell in length constants;  $R_{input}$ , input resistance of cell, including electrode leak.

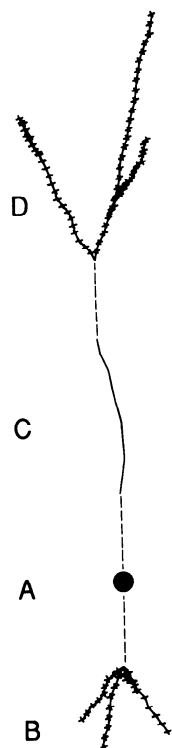


FIG. 6. Regions for granule cell parameter variations. The cell was subdivided into 4 regions, A–D. A, soma; B, deep dendrites; C, trunk; D, peripheral dendrites. As described in the text, these regions were the basis for parameter variations. Within each region, all channel densities are uniform. The values for channel densities are given in Table 3.

on the dendritic spines (Fig. 6) in this model. The effects of including channels on the spines (Fig. 8E) is dealt with in the DISCUSSION.

*Na<sub>gran</sub> and K channels.* These are distributed at high density in the soma and also in the peripheral dendrites. They are present at lower density in the trunk.

*KM channels.* This channel type is modeled in the soma alone. Their presence in the soma is clearly indicated (Yamada et al. 1989) by the increasing interspike interval (Fig. 6A) under conditions of depolarizing current clamp. However, the relatively slow time course and the small electrotonic size of the cell as a whole combine to make it difficult to exclude the possibility that KM channels are also distributed throughout the dendritic arbor. In both cases, the simulations generate similar results (Fig. 7, A and C; Fig. 8, B and D). It is also possible to replicate the increases in interspike interval using a combination of calcium channels, a

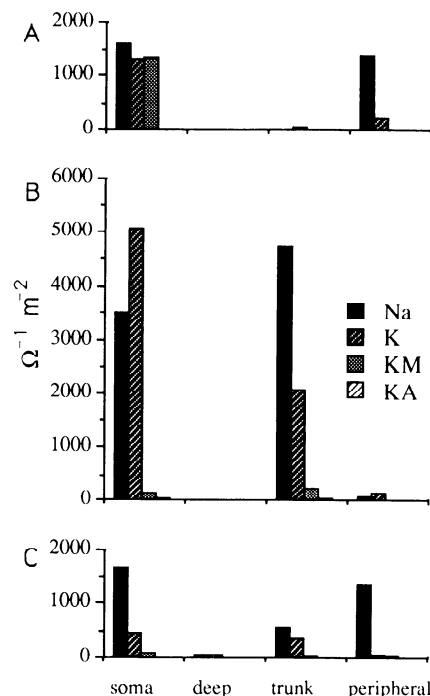


FIG. 7. Channel distributions for 3 granule cell models. These all produced very close matches to experimental data (Fig. 8). Each of the distributions was obtained as the result of an automated parameter search starting from a different initial set of parameters. A: model 1. This model was selected for further analyses because it had the smallest number of channels. B: model 2. This model is unlikely to be correct because of the very high channel densities involved; however, it gives a remarkably good match. The higher channel densities are reflected in the amplitudes and sharpness of the spikes (see Fig. 8C'). C: model 3. This had a more even distribution of rat brain Na channels ( $Na_{gran}$ ) and K channels than the other models over the entire dendritic tree. It gives a good match to experimental data but is computationally expensive.

calcium concentration pool, and calcium-dependent K channels (Yamada et al. 1989). In the absence of further data on channel types and properties for these cells, we have adopted the alternative requiring fewer channel types.

*KA channels.* These are also modeled in the soma. Their presence is indicated by the long slow depolarizing phase of the spike waveform under current clamp (Yamada et al. 1989; Fig. 8).

**APPLYING CELL PARAMETERS TO OTHER CLASSES OF GRANULE CELLS.** We generalized the model for the type I granule cell to the other classes of granule cells, types II and III. We assumed that the differences between the classes were purely in the morphology of the cells, and that the channels were distributed in the same way as in type I cells. As with the mitral cells, the different geometries of the three granule cell classes led to different compartmental decompositions for the cell models.

Morphologically, different types of granule cells differ principally in the distribution of spines. Type I and II cells have spines mainly in the peripheral dendrites of the external plexiform layer, whereas type III granule cells also have spines on the deeper portions of the trunk (Greer 1987). We find that similar channel distributions produce similar spike waveforms for each of the different granule cell geometries (Fig. 9). The differences in geometry and, thus, pas-

TABLE 3. Granule cell channel distributions for model 1

Region	$Na_{gran}$	K	KM	KA
Soma	1,611	1,313	1,334	88
Deep dendrites	0	0	0	0
Trunk	0	71	0	0
Peripheral dendrites	1,355	243	0	0

Channel densities are expressed as Siemens per square meter for the maximum conductance value  $g$  in the rate equation for the channel.  $Na_{gran}$ , rat brain sodium channel; kM, noninactivating muscarinic K channel; for other abbreviations, see Table 1.

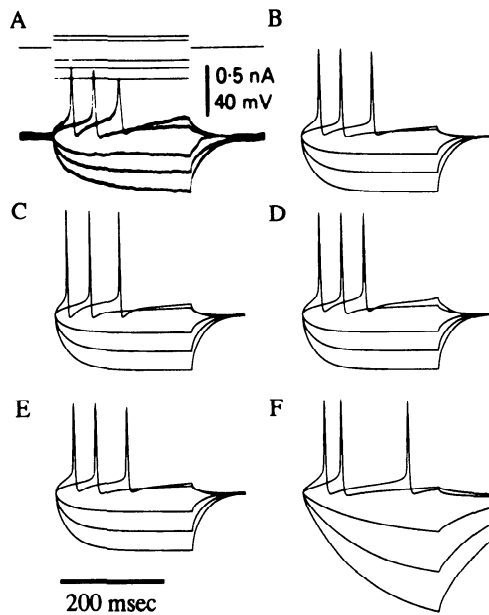


FIG. 8. Experimental and simulated data for granule cell. *A*: experimental data for current-clamp series. (Reproduced with permission from Jahr and Nicoll, 1982.) *B*: simulated data for model 1 of the granule cell, channel distribution as described in Table 3. Frequency limitations of recording apparatus may explain part of difference in spike heights. *C*: simulated data for model 2 of the granule cell. *D*: simulated results for modeled current-clamp series for model 3 of the granule cell. *E*: simulated results for model 1 with active channels modeled on spines rather than dendrites. This waveform is very similar to the waveform in *B*. *F*: simulated results without electrode leak. All injection currents in *F* have been halved to compensate for the increased input resistance of the cell.

sive properties of the cells are reflected in the timing of the spikes (Table 4).

## DISCUSSION

In these modeling experiments, we have demonstrated that the spike waveforms generated by single-neuron models are strongly dependent on channel distributions. Furthermore, the generation of physiologically realistic results requires a particular distribution of channels that may be uniquely determined if sufficient experimental information is available. We have presented a systematic approach to exploring the enormous range of possible parameters that must be specified in any detailed neural simulation study.

The pioneering modeling studies on the olfactory bulb (Rall 1970; Rall and Shepherd 1968) showed that the details of the distribution of voltage-dependent channels have a profound effect both on the behavior of individual neurons and also on the predicted physiological properties of the bulb as a whole. More recent simulations of granule cells and spines (Shepherd and Brayton 1987; Shepherd et al. 1989; Woolf et al. 1991a) have highlighted the role that the details of single-cell morphology and channel distribution may play in information processing. In this context, it is clear that a more complete picture of the active properties of bulbar neurons is a prerequisite to a better understanding of the functioning of the olfactory bulb. The current modeling effort has explored the overall behavior of bulbar neurons using a full complement of active channels under a number of different experimental conditions. The results

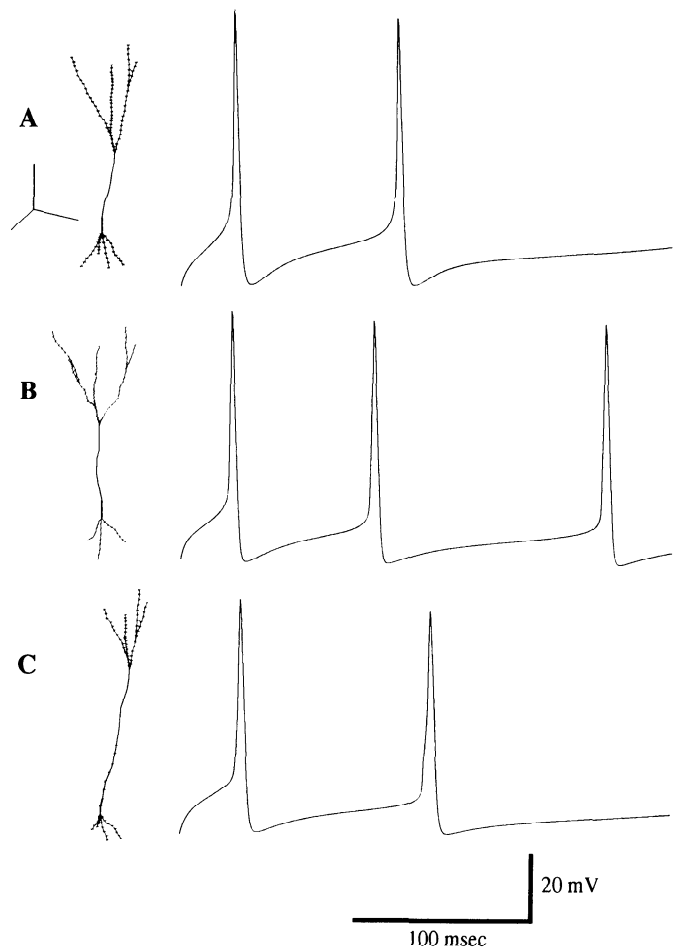


FIG. 9. Different classes of modeled granule cells. *Left* column: cell geometries. Scale bars are 100  $\mu$ m on each axis. *Right* column: responses to current injection of 0.125 nA. All models have assumed electrode leak at soma of 200 M $\Omega$ . *A*: type I granule cell. *B*: type II granule cell. *C*: type III granule cell.

make specific predictions about the distributions of active channels and the physiological consequences of those distributions under specified experimental conditions.

## Electrode leak and passive properties of cells

The objective of this effort was to construct models that reflect the "natural" behavior of these neurons. Accordingly, our models have taken into account the effects of the experimental electrophysiological methods used to obtain the physiological records. Although a complete description of electrode damage would almost certainly have to take into account complex factors such as changes in local ionic concentrations, diffusion, and the cytoskeleton of the cell, we have adopted the convention of previous modeling ef-

TABLE 4. Granule cell model properties

Cell	<i>n</i>	<i>nC</i>	$\tau_0$ , ms	$\tau_1$ , ms	<i>L</i>	$R_{input}$ , M $\Omega$
Type I	944	162	36	3.4	1.0	158.5
Type II	530	182	33	2.7	0.94	166.5
Type III	587	134	34	3.8	1.1	166.8

For abbreviations, see Table 2.



forts (e.g., Segev et al. 1990), and assumed that damage associated with the insertion of a recording electrode into a neuron primarily produces a lowered somatic resistance.

On the basis of data from current injections and input resistance (Mori et al. 1981a), we have included a leak resistance  $R_{\text{leak}}$  of 120 M $\Omega$  in the mitral cell models. A simple calculation shows that this leak resistance would be expected to give a much more depolarized value for final membrane potential than is actually observed. From Ohm's law

$$V_{\text{final}} = E_{\text{rest}} \times (1/(1/R_{\text{leak}} + 1/R_m))$$

$$R_m = -65 \text{ mV} \times 60 \text{ M}\Omega / 120 \text{ M}\Omega = -33 \text{ mV}$$

where  $V_{\text{final}}$  is the potential produced due to the voltage divider formed by the leak and the summed membrane conductance (including the contributions due to channels). This contradiction between predicted and observed resting potentials can be resolved by postulating the presence of ion-selective channels (Pongracz et al. 1991) in addition to the non-ion-selective current due to electrode damage. In our models, a candidate for such a channel might be the noninactivating, voltage-dependent ion channel KM. As has been shown from comparisons of whole-cell patch recordings and conventional intracellular recordings, (Staley et al. 1992), these channels produce a large inward current to compensate for the leak conductance due to electrode damage. Clearly, the approximation of a voltage-dependent channel as a linear membrane resistance is valid only if the kinetics of the compensating current are much slower than any fluctuations of membrane potential. This assumption is very likely to be good for the relatively rapid time courses of neuronal spiking that we are investigating. This condition is not met, however, when long hyperpolarizing current injection pulses are used to estimate membrane time courses. For example, in the granule cell (Fig. 8A), the time course for the hyperpolarizing phase is much longer (by a factor of 2) than the time course for repolarization back to resting potential. Thus the granule cell data is consistent with the postulate that a K current is active at "resting" potentials, thereby affecting the charging curve. For this reason, our calculations of the passive properties of the granule cell model were based on the repolarizing phase of the current pulse, because the current is likely to be inactive at more hyperpolarized potentials (Fig. 8A).

In several simulations, we have removed the electrode leakage current to estimate the response properties of cells that have not been impaled. Under these conditions, we have found very little effect on the spike rates and waveforms produced by the models (Figs. 4F and 8F), when the injection currents are compensated for the change in input resistance. Presumably this lack of effect on cellular output is due to the fact that ionic conductances during an action potential are much larger than the leak conductance introduced by the electrode.

#### *Active channels on mitral cell dendrites*

There is considerable experimental evidence that mitral cell dendrites have active properties. For example, fast prepotentials are observed in mitral cell somas when the olfac-

tory nerve is stimulated (Mori and Takagi 1975; Mori et al. 1981b, 1982). Further, these prepotentials persist when a hyperpolarizing current is simultaneously presented to the soma, suggesting a dendritic origin. Earlier theoretical studies of the bulb (Rall and Shepherd 1968) also proposed active dendrites to match the experimental data then available. Our simulations likewise predict the presence of dendritic spikes, both in the glomerulus and in the secondary dendrites (Figs. 10 and 11). Thus the model supports the previous interpretations of these experimental results.

**PREDICTIONS.** Further exploration of the spike-generating mechanism in the dendrites of mitral cells has suggested an experimental means of further testing the distribution of ion channels predicted here. Specifically, we have found that voltage-clamping the model's soma at depolarizing potentials around spike threshold can reveal several properties of the mitral cell dendrites.

Figure 10A shows the current record produced by the somatic voltage clamp in the model. As can be seen in the axonal voltage recording below the current record, the large current spikes correspond to action potentials generated in the spike initiation zone modeled here in the proximal axonal compartments. However, when this contribution to the current is subtracted (Fig. 10B), a number of small current peaks occurring at different times remain. Comparison of this current record with voltage traces taken from the different dendritic branches reveals that these currents are a direct result of the local active properties of these dendrites. Closer examination of this record reveals current events with two different durations. When the secondary dendritic spikes are also removed from the current trace (Fig. 10C), a correspondence between the broader current peak and the calcium spike in the glomerular tuft and primary dendrite is evident.

If our model is correct, a single-cell voltage clamp near threshold in the soma of a mitral cell should reveal all three types of current events. Our interpretation of this phenomenon is that the large physical and electrotonic size of the mitral cell makes it difficult to generate a good whole-cell space clamp. Consequently, a somatic voltage clamp will only keep regions near the soma at the holding potential, whereas more distal regions are able to vary in potential. As shown in Fig. 10, the active properties of these regions, combined with the spread of depolarization from the near-spike threshold somatic voltage clamp, result in the generation of dendritic electrical events that propagate back to the soma and are seen in the current trace. Further, because the soma is voltage clamped, the large dendrites are effectively decoupled from each other and generate independent events at a rate determined by their individual local properties.

In the context of the current modeling effort, the occurrence of small-amplitude events in the current records of a somatic voltage clamp of a mitral cell would strongly support the existence of active properties in the dendrites of these cells. Recent results from whole-cell recordings from mitral cells (Bufler et al. 1992; D. P. Wellis, personal communication) indicate that such multiple current events are indeed visible. A careful evaluation of the amplitudes and distributions of these spikes might make it possible to deter-

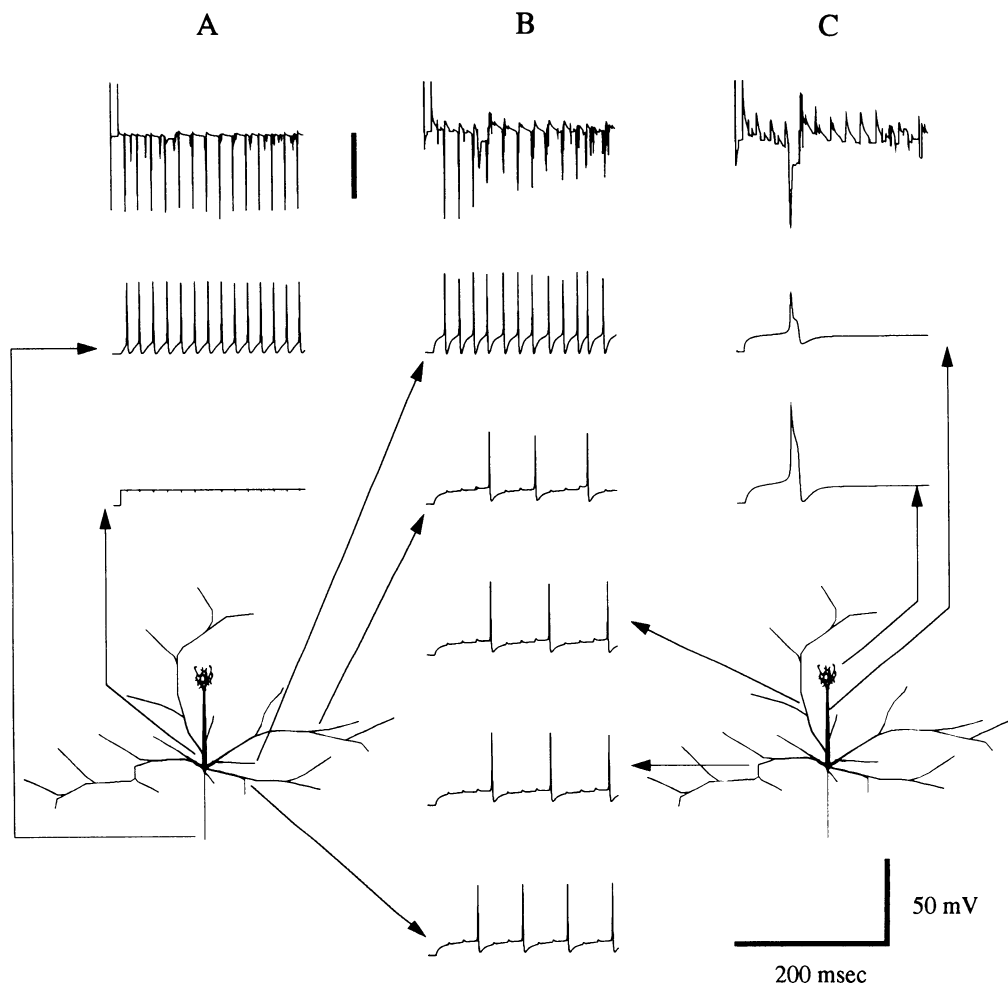


FIG. 10. Voltage clamp at mitral cell soma. Recording sites are indicated on the figures of the mitral cell. *A: top trace:* current recording from voltage-clamp electrode. Scale bar is 20 nA. *Middle trace:* voltage recording at axon. *Bottom trace:* clamped voltage ( $-47.5$  mV) recorded at soma. *B: top trace:* current recording with large axonal spikes subtracted out. Scale bar = 5 nA. *Bottom traces:* recordings from various locations on the secondary dendrites. The spikes are out of synchrony with each other but tend to be individually periodic. *C: top trace:* current recording with axonal and secondary dendritic spikes removed. Scale bar = 2 nA. *Middle trace:* recording from primary dendrite. *Bottom trace:* recording from glomerular tuft. The much wider calcium spike is reflected in the width of the corresponding current event.

mine whether there are differential thresholds for spiking activity in different dendrites. This, in turn, might indicate different electrotonic distances of the dendrites from the point of voltage clamp, or different local channel distributions. Distinguishing between these possibilities, however, will require further detailed simulations of the sort described here.

**FUNCTIONAL SIGNIFICANCE.** On the basis of several studies demonstrating prepotentials (Jahr and Nicoll 1982; Mori and Takagi 1975; Mori et al. 1982; Wellis et al. 1989), the mitral cell glomerular tuft is believed to possess active channels. Taken in conjunction with the electrotonic distance of the tuft from the mitral cell soma, this has led to general agreement that the glomerular tuft may take part in local processing and amplification of incoming synaptic input from the olfactory nerve (Jahr and Nicoll 1982; Mori et al. 1982; Rall and Shepherd 1968; Wellis et al. 1989). Our simulations also incorporate active channels in the primary dendrites and are consistent with this view. We also observe that, in addition to the amplification of synaptic input, the

active channels in the glomerular tuft lead to interesting interactions with somatic spikes.

In the nonphysiological situation where spikes are being initiated at the soma by current clamp or antidromic stimuli, action potentials may propagate into the glomerulus to initiate a calcium spike (Fig. 11C). This process depends on the previous level of depolarization in the tuft. The long-lasting depolarization due to the calcium spike in the glomerular tuft may cause the initiation of a second somatic spike. Thus the model predicts a conditional propagation of spikes into the glomerulus from the soma, and vice versa, depending on the state of the cell. Similar interactions between dendritic calcium spikes and somatic action potentials has also been modeled in several other neuronal classes such as hippocampal pyramidal neurons (Traub and Llinas 1979) and Purkinje cells from the cerebellum (De Schutter and Bower 1991).

In a more physiological context, our model clearly suggests that the presence of active channels in mitral cell dendrites should support the propagation of somatic action po-



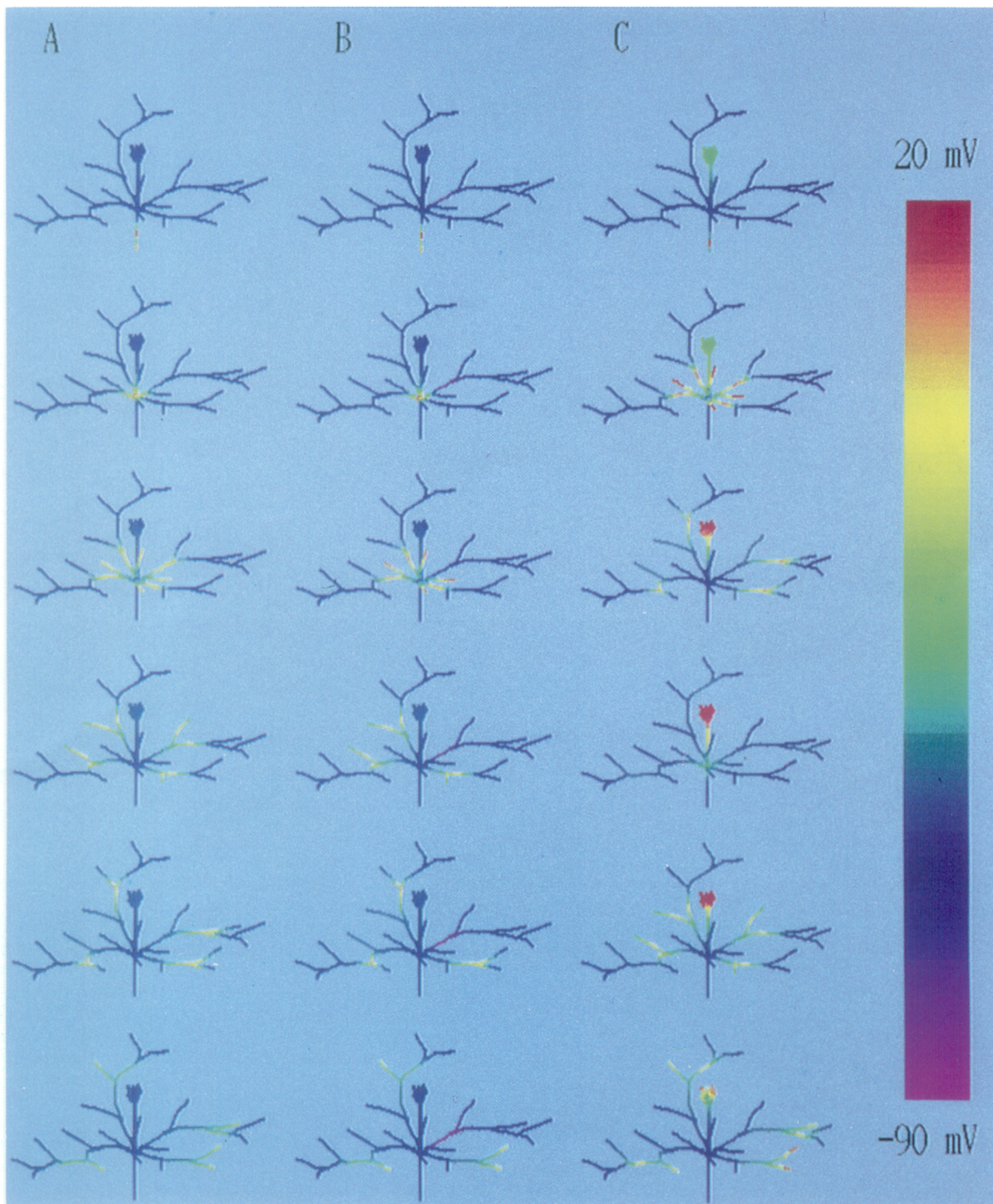


FIG. 11. Spike propagation into mitral cell dendrites. *A*: antidromic stimulation of mitral cell, shown at 1.5-ms intervals. *B*: failure of spike propagation into secondary dendrite. Antidromic stimulation on axon, with hyperpolarization (0.5-nA current injection) on secondary dendrite 1 (in the 1st quadrant with respect to the soma). Shown at 1.5-ms intervals. *C*: antidromic stimulation with glomerular tuft initially depolarized to -20 mV. The somatic spike leads to a glomerular dendritic calcium spike, which causes a 2nd somatic spike. Shown at 3.0-ms intervals.



tentials into the secondary dendrites (Fig. 11*A*). This propagation has been previously considered in modeling studies (Rall and Shepherd 1968), but interpretations were deferred pending additional experiments. Such dendritic spike propagation is very interesting when considered in the context of the dendrodendritic synapses known to occur between mitral cell secondary dendrites and granule cells (e.g., Mori 1987; Rall and Shepherd 1968). In effect, these dendrites may act rather like axons in conveying information in an all-or-nothing manner to the granule cells. One manifestation of this sort of all-or-nothing behavior is seen in intracellular recordings from mitral cells with paired-pulse stimulation of the lateral olfactory tuft (e.g., Mori and Takagi 1978). In this case, the second pulse fails to elicit a somatic spike, and the inhibitory postsynaptic potential at the mitral cell soma due to the second pulse is depressed. This is interpreted as a reduction in the dendrodendritic inhibition from the granule cell due to the spike blockage at the mitral cell soma (Rall and Shepherd 1968). Our model suggests that a similar but finer control may be exerted at the level of the individual secondary dendritic branch. For example, as shown in Fig. 11, *A* and *B*, action potential propagation is quite sensitive to the previous membrane potential of local regions of the dendrite. As a result, spike propagation into secondary dendrites can be blocked by a local hyperpolarization (Fig. 11*B*). In this way, inhibitory feedback from granule cells could block spike propagation along individual mitral cell secondary dendrites and thereby alter the information received by granule cells in contact with those branches at points more distant from the soma. Theoretical studies (Manor et al. 1991) have investigated the computational implications of conditional failure of spike propagation in axons. Such a blockage of spikes propagating outward from the soma along individual dendrites, if correct, would be a form of information processing that has not yet been described in other parts of the mammalian CNS.

#### *Active channels on granule cell dendrites*

As mentioned earlier, there have been many speculations on the role of active channels in granule cell dendrites, and their precise location, on the computational role of these cells (Rall and Shepherd 1968; Shepherd and Brayton 1987; Shepherd et al. 1989; Woolf et al. 1991a,b). Our present study is confined to single-cell models, and therefore does not address many of these issues directly. We have used our granule cell model to test whether any predictions could be made about the exact location of active channels on the spines or on their parent dendrites. Specifically, under somatic current clamp we held the total conductance due to the respective ion channels fixed while placing channels on either the dendrites or on the spine heads emerging from them. The results, shown in Fig. 8*E*, indicate that one cannot differentiate between these two possibilities using the simple somatic current-clamp approach.

#### *Whole-bulb models*

Ultimately, understanding the interaction of the active properties of the mitral cell on the granule cell and the consequences of this interaction on the computation per-

formed by the olfactory bulb will require the study of network models of the entire bulb (Anton et al. 1991; Freeman et al. 1988; Li and Hopfield 1989; Meredith 1992; Rall 1970; Rall and Shepherd 1968; Schild and Riedel 1992; White et al. 1992). In this regard, the single-cell modeling effort just described is a preliminary step toward the development of detailed, realistic models of the bulb as a whole. Many of the questions raised by single-cell recordings are best addressed in the context of a network, where the ramifications of active neuronal properties can be more fully explored. This effort will undoubtedly further illuminate the complexities of these cells as well as the network in which they are embedded.

#### *Conclusions*

These simulations have made both general and specific predictions about voltage-dependent channel distributions in the dendrites of mitral and granule cells. The results confirm interpretations of previous experimental work as well as make specific experimental predictions that can be used to further experimentally test the accuracy of the models. Further, they suggest several functional consequences for the processing performed in these cells.

Beyond the significance of model results for function of the olfactory bulb, in this paper we have also presented a more thorough than usual search of model parameter space. The more complete mitral cell results suggest that real neurons may operate in ranges that are relatively robust with respect to physical variations. In some cases, for example, differences in channel densities of up to an order of magnitude produce relatively little change in the model output. Substantial changes in membrane properties, such as the presence or absence of electrode leak at the soma, were also shown to cause relatively small effects on the spike waveforms. Even applying the calculated channel distributions to substantially different morphologies, for different classes of mitral and granule cells, does not markedly affect the spiking properties of the cell models.

We believe these results have important implications for future modeling efforts. First, the search for the "correct" model can only be conducted up to a certain level of precision, because members of the same class of neurons may experience variability below that level. Second, there are likely to be whole classes of models that are all equally correct as far as reproducing the data is concerned. In the absence of further experimental data constraining the model one way or another, considerations of aesthetics, efficiency, or ideas about function will continue to decide the model chosen. We believe it is the modeler's obligation to indicate, as far as possible, the range of models that might fit the data.

#### APPENDIX A: QUANTITATIVE COMPARISON OF MODELED AND REAL DATA

To automate the parameter search, it is necessary to quantify the similarity between simulated and experimental data for each set of parameters. The goodness of our model parameters is evaluated by running a simulation using those parameters under the appropriate experimental conditions. The output from this simulation then has to be compared with intracellular voltage recordings

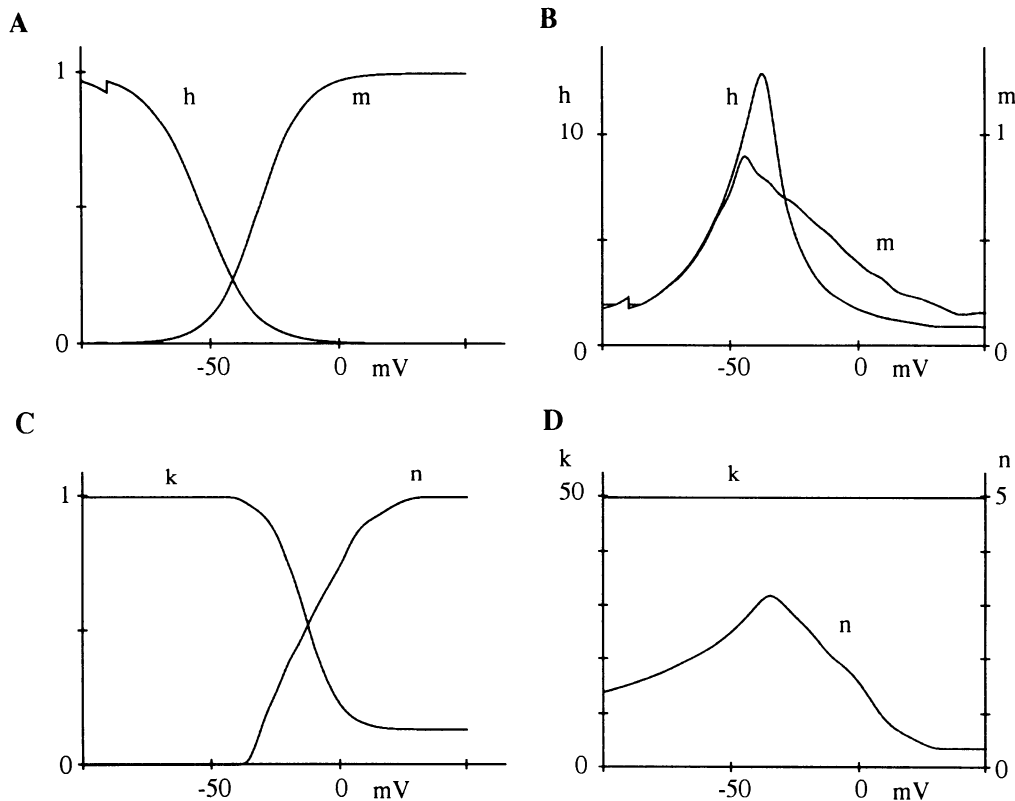


FIG. 12. Channel parameters. *A*:  $m_{\infty}$  and  $h_{\infty}$  curves for Na<sub>gran</sub> channel. *B*:  $\tau$  curves for Na<sub>gran</sub> channel. *C*:  $n_{\infty}$  and  $k_{\infty}$  curves for Kfast and K channels. The small jump in the curves at  $-90$  mV is due to an error in the scaling routines for the kinetics. The cells almost never encounter values in this range. *D*:  $\tau$  curves for Kfast and K channels. The K channel has slower kinetics, but the shapes of the curves are identical to Kfast. The  $\tau$  values for K are scaled up by a factor of 4 from the graph. For all calculations outside the tabulated voltage range, the values for the extreme points are used.

and some measure of similarity evaluated. The measure of match we use here is computed by comparing a number of different features of the simulated and reference waveforms. These include:

1) Shape of voltage waveforms  $V_{ref}$  and  $V_{sim}$ . The nonspiking phase of each spike waveform is scaled to match on the time axis and directly compared using root-mean-squared difference over all the sample points. Linear interpolation is used when the sampling intervals for the two curves are different. The root-mean-squared value is normalized to a typical spike amplitude of 100 mV (0.1 V in the equation because the simulation uses SI units). The additional square root is an empirical means of keeping the scaling commensurate with the other measures

$$Shape\_match = \sqrt[3]{(\sum (V_{ref} - V_{sim})^2) / (0.1 n_{points})}$$

2) Interspike intervals  $ISI_{ref}$  and  $ISI_{sim}$ . The time between spikes is calculated and corresponding intervals are compared. The interspike intervals are compared as the sum of the ratio and inverse ratio to ensure that all changes from unity result in an increase in the measure of difference. The final sum is normalized to the number of spikes and scaled as an inverse exponential to keep the scaling commensurate with the other measures

$$ISI\_match = 1 - \exp(-(\sum (ISI_{ref}/ISI_{sim} + ISI_{sim}/ISI_{ref} - 2) / n_{spikes}))$$

3) Peak-to-peak amplitudes  $PTP_{ref}$  and  $PTP_{sim}$ . The amplitudes of corresponding spikes are compared using root mean squared

$$PTP\_match = (\sqrt{\sum (PTP_{ref} - PTP_{sim})^2}) / n_{spikes}$$

These three measures of spike waveform similarity are combined using weighting factors determined by the user. We have also used other matching functions, which give similar results for parameter searches.

## APPENDIX B: AUTOMATED SEARCHING OF PARAMETER SPACE

There are at least three commonly used numerical methods for exploring parameter space: brute force, a systematic search based on successive approaches to the final point, and Monte Carlo methods. Our study has employed the first two.

### Brute force parameter searches

If each dimension in parameter space is sampled at a fixed number of points, one can in principle exhaustively evaluate every sample point in the parameter space. However, this rapidly becomes intractable for large parameter spaces, such as in our models. For example, in the mitral cell, we use six channel types and subdivide the cell into six regions, giving a total of 36 parameters. To search such a parameter space even at a very coarse sampling of six values per dimension, we would require  $6^{36}$  ( $\sim 10^{28}$ ) simulations. To reduce the number of simulations to a more tractable value, we have adopted the following simplifications:

1) Intrinsic model constraints. Experimental information often enables one to eliminate large numbers of parameters from consideration. For example, in the mitral cell model under conditions of TEA and TTX application, two classes of channel (Na and Kfast) were assumed to be completely blocked. This reduces the number of free parameters from 36 to 24.

2) Lumping regions together. For the purposes of searching, one can choose to lump certain regions of the cell together and vary the channel densities uniformly within the lumped regions. We were able to perform searches of 6 parameters at six sample points per parameter or 10 parameters at three sample points per parameter

(~50,000 simulations each). This method is intrinsically crude and is only useful for roughly localizing regions of interest in parameter space.

3) Plane sections through parameter space. This method involves searches of pairs of parameters to generate plane sections of parameter space. Typical numbers for this case are 32 samples for each parameter and ~50 combinations of parameter pairs (again, ~50,000 simulations). This method is only useful when one is already in the vicinity of the expected minimum and wishes to obtain an estimate of the robustness of the solution.

### Systematic searches using conjugate gradients

Conjugate gradient methods involve successive computations of local gradients followed by exploration of the space along a vector determined from that gradient. A number of variations of this approach exist. We have developed a modification of the Fletcher-Reeves-Polack-Ribiere method (Press et al. 1988), which is suited to parallelization. Gradients are evaluated for each dimension using two sample points to smooth out the slopes. On the basis of the gradient, the algorithm selects a vector in parameter space, passing through the initial point. The best value of match along this selected vector is evaluated on the basis of a fixed number of sample points and B-spline interpolation (Enns 1986). This match point becomes the starting point for another cycle of the gradient method.

Each of these cycles involves many independent calculations of match based on parameters determined at the outset of the stage. This allows one to compute each iteration in the same amount of time as required for a single simulation by farming out the desired parameters to a large number of independent nodes on a parallel computer. Conjugate gradient methods are extremely efficient, usually converging within five or so cycles, as described above (typically 200–300 simulations).

### Combination of parameter searching methods

Basic conjugate gradient methods assume that there is a unique solution to the problem, and that the energy (matching) function is smooth. Neither of these conditions is met for our neuronal parameter searching problem. We have therefore combined conjugate gradient with brute force methods to obtain solutions that are very likely to be reliable. Initial parameter searches are usually done using brute force methods. When an approximate idea of the correct region of parameter space is available, one can use the gradient scheme. This is typically done using different weighting functions and starting points, to check if there is a common solution to which all these converge. Finally, plane sections of parameter space are used to determine the smoothness of nearby parameter space and to estimate the robustness of the solution.

## APPENDIX C: CHANNEL PARAMETERS

The Hodgkin-Huxley formalism is used for all channels. Two alternative forms, the  $\alpha$ - $\beta$  form (Eq. 2) and the  $\tau$ - $m_\infty$  form (Eq. 3) are used to describe the channel kinetics. For three channels,  $\text{Na}_{\text{gran}}$ , Kfast and K, the kinetics have not been reduced to analytical form and are therefore described by plots of the voltage dependencies of their kinetics (Fig. 12).

Voltage units: millivolts, with respect to extracellular potential. The resting potential is -65 mV for all cells. Time units: milliseconds. Resistance units: megohms. Concentration units: millimoles per liter.

1) Compartment equation.  $i$  refers to the index of the present compartment,  $j$  is the index for the ionic conductance  $g_j$  with reversal potential  $E_j$ . The remaining terms have been defined in the text

$$Cm_i dV_i/dt = (Em_i - V_i)/Rm_i + (V_{i+1} - V_i)/(Ra_{i,i+1}) + (V_{i-1} - V_i)/(Ra_{i,i-1}) + \Sigma g_j(E_j - V_i)$$

2) Dependence of gating parameter  $m$  on rate constants  $\alpha$  and  $\beta$

$$dm/dt = \alpha_m(1 - m) - \beta_m m$$

3) Dependence of gating parameter  $m$  on rate constants  $\tau$  and  $m_\infty$

$$dm/dt = (m_\infty - m)/\tau_m$$

4) Mitral Na channel

$$g_{\text{Na}} = \bar{g}_{\text{Na}} m^3 h$$

$$\alpha_m = 0.32(V + 42)/(1 - \exp(-(V + 42)/4))$$

$$\beta_m = 0.28(V + 15)/(\exp((V + 15)/5) - 1)$$

$$\alpha_h = 0.128/\exp((V + 38)/18)$$

$$\beta_h = 4/(1 + \exp(-(V + 15)/5))$$

5) Granule Na channel. See Fig. 12, *A* and *B*

$$g_{\text{Nagran}} = \bar{g}_{\text{Nagran}} m^3 h$$

6) Mitral Ca channel

$$g_{\text{Ca}} = \bar{g}_{\text{Ca}} s^r$$

$$\alpha_s = 7.5/(1 + \exp((13 - V)/7))$$

$$\beta_s = 1.65/(1 + \exp((V - 14)/4))$$

$$\alpha_r = 6.8 \times 10^{-3}/(1 + \exp((V + 30)/12))$$

$$\beta_r = 0.06/(1 + \exp(-V/11))$$

7) Mitral Kfast channel. See Fig. 12, *C* and *D*

$$g_{\text{Kfast}} = \bar{g}_{\text{Kfast}} n^2 k$$

8) Mitral and granule cell K channel. See Fig. 12, *C* and *D*. The  $\tau$  parameters are slower (larger) by a factor of 4 from the values in the figure

$$g_{\text{K}} = \bar{g}_{\text{K}} n^2 k$$

9) Mitral and granule cell K A channel

$$g_{\text{KA}} = \bar{g}_{\text{KA}} p^q$$

$$\tau_p = 1.38$$

$$p_\infty = 1/(1 + \exp(-(V + 42)/13))$$

$$\tau_q = 150$$

$$q_\infty = 1/(1 + \exp((V + 110)/18))$$

10) Granule cell KM channel

$$g_{\text{KM}} = \bar{g}_{\text{KM}} \chi$$

$$\tau_\chi = 1000/(3.3 \exp((V + 35)/40) + \exp(-(V + 35)/20))$$

$$\chi_\infty = 1/(1 + \exp(-(V + 35)/5))$$

11) Mitral K<sub>Ca</sub> channel.  $\chi$  represents calcium ion concentration

$$g_{\text{KCa}} = \bar{g}_{\text{KCa}} \chi^y$$

$$\alpha_y = \exp((V - 65)/27) \times (500(0.015 - \chi)/$$

$$(\exp((0.015 - \chi)/0.0013) - 1)$$

$$\beta_y = 0.05$$

The authors are grateful to Dr. Erik De Schutter for many helpful discussions and valuable insights into these modeling efforts. The early phase of this work owes a great deal to the assistance of Drs. Matt Wilson and Mark Nelson. The port of GENESIS to the Delta, on which many of these simula-



tions were performed, was carried out by Dr. Michael Speight. We also thank D. Bilitch and J. Uhley for technical assistance.

This work was supported by Office of Naval Research contract N00014-88-K-0513 and National Science Foundation Grant DIR 9017153.

Address reprint requests to J. M. Bower.

Received 19 August 1992; accepted in final form 15 January 1993.

## REFERENCES

- ADAMS, D. J., SMITH, S. J., AND THOMPSON, S. H. Ionic currents in molluscan soma. *Annu. Rev. Neurosci.* 3: 141–167, 1980.
- ALDRICH, R. W., JR., GETTING, P. A., AND THOMPSON, S. H. Inactivation of delayed outward current in molluscan neurone somata. *J. Physiol. Lond.* 291: 507–530, 1979.
- ANTON, P. S., LYNCH, G., AND GRANGER, R. Computation of frequency-to-spatial transform by olfactory bulb glomeruli. *Biol. Cybern.* 65: 407–414, 1991.
- BELLUZZI, O. AND SACCHI, O. A five-conductance model of the action potential in the rat sympathetic neurone. *Prog. Biophys. Mol. Biol.* 55: 1–30, 1991.
- BHALLA, U. S., BILITCH, D. H., AND BOWER, J. M. Rallpacks: a set of benchmarks for neuronal simulators. *Trends Neurosci.* 15: 453–458, 1992.
- BUFLER, J., ZUFALL, F., FRANKE, C., AND HATT, H. Patch-clamp recordings of spiking and nonspiking interneurons from rabbit olfactory bulb slices: membrane properties and ionic currents. *J. Comp. Physiol. A Sens. Neural Behav. Physiol.* 170: 145–152, 1992.
- CONNOR, J. A. AND STEVENS, C. F. Prediction of repetitive firing behaviour from voltage clamp data on an isolated neurone soma. *J. Physiol. Lond.* 213: 31–53, 1971.
- COOLEY, J. W. AND DODGE, F. A. Digital computer solutions for excitation and propagation of the nerve impulse. *Biophys. J.* 6: 583–599, 1966.
- DE SCHUTTER, E. AND BOWER, J. M. A computer simulation of plateau potentials and synaptic interactions in Purkinje cell spiny dendrites. *Soc. Neurosci. Abstr.* 21: 1383, 1991.
- EGAN, T. M., DAGAN, D., KUPPER, J., AND LEVITAN, I. B. Properties and rundown of sodium-activated potassium channels in rat olfactory bulb neurons. *J. Neurosci.* 12: 1964–1976, 1992.
- ENNS, S. Free-form curves on your micro. *Byte* 12: 225–230, 1986.
- FITZHUGH, R. Impulses and physiological states in theoretical models of nerve membrane. *Biophys. J.* 1: 445–466, 1961.
- FREEMAN, W. J., YAO, Y., AND BURKE, B. Central pattern generating and recognizing in olfactory bulb: a correlation learning rule. *Neural Networks* 1: 277–288, 1988.
- GREER, C. A. Golgi analysis of dendritic organization among denervated olfactory bulb granule cells. *J. Comp. Neurol.* 257: 442–452, 1987.
- HABERLY, L. AND PRICE, J. L. The axonal projection patterns of the mitral and tufted cells of the olfactory bulb in the rat. *Brain Res.* 129: 152–157, 1977.
- HINES, M. Efficient computation of branched nerve equations. *Int. J. Bio-Med. Comput.* 15: 69–76, 1984.
- HIRANO, T. AND HAGIWARA, S. Kinetics and distribution of voltage-gated Ca, Na and K channels on the somata of rat cerebellar Purkinje cells. *Pfluegers Arch.* 413: 463–469, 1989.
- HODGKIN, A. L. AND HUXLEY, A. F. A quantitative description of membrane current and its application to conduction and excitation in nerve. *J. Physiol. Lond.* 117: 500–544, 1952.
- JACK, J. J. B., NOBLE, D., AND TSUEN, R. W. *Electric Current Flow in Excitable Cells*. Oxford, UK: Oxford Univ. Press, 1983.
- JAHR, C. E. AND NICOLL, R. A. An intracellular analysis of dendrodendritic inhibition in the turtle in vitro olfactory bulb. *J. Physiol. Lond.* 326: 213–234, 1982.
- KOCH, C. AND BOWER, J. M. Experimentalists and modelers: can we all just get along? *Trends Neurosci.* 15: 458–461, 1992.
- LI, Z. AND HOPFIELD, J. J. Modeling the olfactory bulb and its neural oscillatory processing. *Biol. Cybern.* 61: 379–392, 1989.
- MANOR, Y., GONCZAROWSKI, J., AND SEGEV, I. Propagation of action potentials along complex axonal trees. Model and implementation. *Biophys. J.* 60: 1411–1423, 1991.
- MASCAGNI, M. Numerical methods for neuronal modeling. In: *Methods in Neuronal Modeling: From Synapses to Networks*, edited by C. Koch and I. Segev. Cambridge, MA: MIT Press, 1989, p. 439–484.
- MEREDITH, M. Neural circuit computation: complex patterns in the olfactory bulb. *Brain Res. Bull.* 29: 111–117, 1992.
- MORI, K. Membrane and synaptic properties of identified neurons in the olfactory bulb. *Prog. Neurobiol.* 29: 275–320, 1987.
- MORI, K. AND KISHI, K. The morphology and physiology of the granule cells in the rabbit olfactory bulb revealed by intracellular recording and HRP injection. *Brain Res.* 247: 129–133, 1982.
- MORI, K., KISHI, K., AND OJIMA, H. Distribution of dendrites of mitral, displaced mitral, tufted, and granule cells in the rabbit olfactory bulb. *J. Comp. Neurol.* 219: 339–355, 1983.
- MORI, K., NOWICKY, M. C., AND SHEPHERD, G. M. Electrophysiological analysis of mitral cells in the isolated turtle olfactory bulb. *J. Physiol. Lond.* 314: 281–294, 1981a.
- MORI, K., NOWICKY, M. C., AND SHEPHERD, G. M. Analysis of synaptic potentials in mitral cells in the isolated turtle olfactory bulb. *J. Physiol. Lond.* 314: 295–309, 1981b.
- MORI, K., NOWICKY, M. C., AND SHEPHERD, G. M. Impulse activity in presynaptic dendrites: analysis of mitral cells in the isolated turtle olfactory bulb. *J. Neurosci.* 2: 497–502, 1982.
- MORI, K. AND TAKAGI, S. F. Spike generation in the mitral cell dendrite in the rabbit olfactory bulb. *Brain Res.* 100: 685–689, 1975.
- MORI, K. AND TAKAGI, S. F. An intracellular study of dendrodendritic inhibitory synapses on mitral cells in the rabbit olfactory bulb. *J. Physiol. Lond.* 279: 569–588, 1978.
- NICKELL, W. T., BEHBEHANI, M. M., AND SHIPLEY, M. T. In vitro synaptic activation of adult rat olfactory bulb mitral cells recorded by conventional and whole cell patch techniques. *Soc. Neurosci. Abstr.* 18: 1200, 1992.
- PONGRACZ, F., FIRESTEIN, S., AND SHEPHERD, G. M. Electrotonic structure of olfactory sensory neurons analyzed by intracellular and whole cell patch techniques. *J. Neurophysiol.* 65: 747–758, 1991.
- PRESS, W. H., FLANNERY, B. P., TEUKOLSKY, S. A., AND VETTERLING, W. T. *The Art of Scientific Computing*. Cambridge, UK: Cambridge Univ. Press, 1988.
- PRICE, J. L. AND POWELL, T. P. S. The morphology of the granule cells of the olfactory bulb. *J. Cell Sci.* 7: 91–123, 1970a.
- PRICE, J. L. AND POWELL, T. P. S. The mitral and short axon cells of the olfactory bulb. *J. Cell Sci.* 7: 631–651, 1970b.
- RALL, W. Branching dendritic trees and motoneuron membrane resistivity. *Exp. Neurol.* 1: 491–527, 1959.
- RALL, W. Theoretical significance of dendritic trees for neuronal input-output relations. In: *Neural Theory and Modeling*, edited by R. Reiss. Stanford, CA: Stanford Univ. Press, 1964, p. 73–97.
- RALL, W. Time constants and electrotonic length of membrane cylinders and neurons. *Biophys. J.* 9: 1483–1508, 1969.
- RALL, W. Dendritic neuron theory and dendrodendritic synapses in a simple cortical system. In: *The Neurosciences. Second Study Program*, edited by F. O. Schmitt. New York: Rockefeller Univ. Press, 1970, p. 552–565.
- RALL, W. Core conductor theory and cable properties of neurons. In: *Handbook of Physiology. The Nervous System. Cellular Biology of Neurons*. Bethesda, MD: Am. Physiol. Soc., 1977, sect. 1, vol. 1, p. 39–97.
- RALL, W. Perspectives on neuron modeling. In: *The Segmental Motor System*, edited by M. D. Binder and L. M. Mendell. New York: Oxford Univ. Press, 1990, p. 129–149.
- RALL, W. AND RINZEL, J. Branch input resistance and steady attenuation for input to one branch of a dendritic neuron model. *Biophys. J.* 13: 648–688, 1973.
- RALL, W. AND SHEPHERD, G. M. Theoretical reconstruction of field potentials and dendrodendritic synaptic interactions in olfactory bulb. *J. Neurophysiol.* 31: 884–915, 1968.
- RALL, W., SHEPHERD, G. M., REESE, T. S., AND BRIGHTMAN, M. W. Dendrodendritic synaptic pathway for inhibition in the olfactory bulb. *Exp. Neurol.* 14: 44–56, 1966.
- SCHILD, D., AND RIEDEL, H. Significance of glomerular compartmentalization for olfactory coding. *Biophys. J.* 61: 704–715, 1992.
- SCHWARTZKROIN, P. A. Secondary range rhythmic spiking in hippocampal neurons. *Brain Res.* 149: 247–250, 1978.

- SEGEV, I., FLESHMAN, J. W., AND BURKE, R. E. Computer simulation of group 1a EPSPs using morphologically realistic models of cat a-motoneurons. *J. Neurophysiol.* 64: 648–660, 1990.
- SHEPHERD, G. M. Canonical neurons and their computational organization. In: *Single Neuron Computation*, edited by T. McKenna, J. Davis, and S. F. Zornetzer. San Diego, CA: Academic, 1992, p. 27–60.
- SHEPHERD, G. M. AND BRAYTON, R. K. Logic operations are properties of computer-simulated interactions between excitable dendritic spines. *Neuroscience* 21: 151–165, 1987.
- SHEPHERD, G. M., WOOLF, T. B., AND CARNEVALE, N. T. Comparisons between active properties of distal dendritic branches and spines: implications for neuronal computations. *J. Cog. Neurosci.* 1: 273–286, 1989.
- STALEY, K. J., OTIS, T. S., AND MODY, I. Membrane properties of dentate gyrus granule cells: comparison of sharp microelectrode and whole-cell recordings. *J. Neurophysiol.* 67: 1346–1358, 1992.
- STUHMER, W., METHFESSEL, C., SAKMANN, B., NODA, M., AND NUMA, S. Patch clamp characterization of sodium channels expressed from rat brain cDNA. *Eur. Biophys. J.* 14: 131–138, 1987.
- TRAUB, R. D. AND LLINAS, R. Hippocampal pyramidal cells: significance of dendritic ionic conductances for neuronal function and epileptogenesis. *J. Neurophysiol.* 42: 476–496, 1979.
- TRAUB, R. D. Simulation of intrinsic bursting in CA3 hippocampal neurons. *Neuroscience* 7: 1233–1242, 1982.
- TROMBLEY, P. Q. AND SHEPHERD, G. M. Noradrenergic inhibition of synaptic transmission between mitral and granule cells in mammalian olfactory bulb cultures. *J. Neurosci.* 12: 3985–3991, 1992.
- WELLIS, D. P. AND SCOTT, J. W. Intracellular responses of identified at olfactory bulb interneurons to electrical and odor stimulation. *J. Neurophysiol.* 64: 932–947, 1990.
- WELLIS, D. P., SCOTT, J. W., AND HARRISON, T. A. Discrimination among odorants by single neurons of the rat olfactory bulb. *J. Neurophysiol.* 61: 1161–1177, 1989.
- WHITE, J., HAMILTON, K. A., NEFF, S. R., AND KAUER, J. S. Emergent properties of odor information coding in a representational model of the salamander olfactory bulb. *J. Neurosci.* 12: 1772–1780, 1992.
- WILSON, M. A., BHALLA, U. S., UHLEY, J. D., AND BOWER, J. M. Genesis: a system for simulating neural networks. In: *Advances in Neural Information Processing Systems, Vol I*, edited by D. Touretzky. San Mateo: Morgan Kaufman, 1989, p. 485–492.
- WILSON, M. AND BOWER, J. M. Cortical oscillations and temporal interactions in a computer simulation of piriform cortex. *J. Neurophysiol.* 67: 981–995, 1992.
- WOOLF, T. B., SHEPHERD, G. M., AND GREER, C. A. Local information processing in dendritic trees: subsets of spines in granule cells of the mammalian olfactory bulb. *J. Neurosci.* 11: 1837–1854, 1991a.
- WOOLF, T. B., SHEPHERD, G. M., AND GREER, C. A. Serial reconstructions of granule cell spines in the mammalian olfactory bulb. *Synapse* 7: 181–192, 1991b.
- YAMADA, W. M., KOCH, C., AND ADAMS, P. R. Multiple channels and calcium dynamics. In: *Methods in Neuronal Modeling: From Synapses to Networks*, edited by C. Koch and I. Segev. Cambridge, MA: MIT Press, 1989, p. 97–133.
- YUEN, G. L. F. AND DURAND, D. Reconstruction of hippocampal granule cell electrophysiology by computer simulation. *Neuroscience* 41: 411–423, 1991.